

# Handbook of Advanced Manufactured Material Properties from TCR Structure Builds at ORNL—FY 2019



K. G. Field  
J. Simpson  
M. N. Gussev  
H. Wang  
M. Li  
X. Zhang  
X. Chen  
T. Koyanagi  
K. Kane  
A. Marquez Rossy  
M. Balooch  
K. A. Terrani

**September 20, 2019**

M3CT-19OR06090121

## DOCUMENT AVAILABILITY

Reports produced after January 1, 1996, are generally available free via US Department of Energy (DOE) SciTech Connect.

**Website** [www.osti.gov](http://www.osti.gov)

Reports produced before January 1, 1996, may be purchased by members of the public from the following source:

National Technical Information Service  
5285 Port Royal Road  
Springfield, VA 22161  
**Telephone** 703-605-6000 (1-800-553-6847)  
**TDD** 703-487-4639  
**Fax** 703-605-6900  
**E-mail** [info@ntis.gov](mailto:info@ntis.gov)  
**Website** <http://classic.ntis.gov/>

Reports are available to DOE employees, DOE contractors, Energy Technology Data Exchange representatives, and International Nuclear Information System representatives from the following source:

Office of Scientific and Technical Information  
PO Box 62  
Oak Ridge, TN 37831  
**Telephone** 865-576-8401  
**Fax** 865-576-5728  
**E-mail** [reports@osti.gov](mailto:reports@osti.gov)  
**Website** <http://www.osti.gov/contact.html>

This report was prepared as an account of work sponsored by an agency of the United States Government. Neither the United States Government nor any agency thereof, nor any of their employees, makes any warranty, express or implied, or assumes any legal liability or responsibility for the accuracy, completeness, or usefulness of any information, apparatus, product, or process disclosed, or represents that its use would not infringe privately owned rights. Reference herein to any specific commercial product, process, or service by trade name, trademark, manufacturer, or otherwise, does not necessarily constitute or imply its endorsement, recommendation, or favoring by the United States Government or any agency thereof. The views and opinions of authors expressed herein do not necessarily state or reflect those of the United States Government or any agency thereof.

Transformational Challenge Reactor

**HANDBOOK OF ADVANCED MANUFACTURED MATERIAL PROPERTIES FROM  
TCR STRUCTURE BUILDS AT ORNL— FY 2019**

K. G. Field<sup>a</sup>  
J. Simpson<sup>a</sup>  
M. N. Gussev<sup>a</sup>  
H. Wang<sup>a</sup>  
X. Xhen<sup>a</sup>  
T. Koyanagi<sup>a</sup>  
K. Kane<sup>a</sup>  
A. Marquez Rossy<sup>a</sup>  
M. Balooch<sup>a</sup>  
K. A. Terrani<sup>a</sup>  
M. Li<sup>b</sup>  
X. Zhang<sup>b</sup>

---

<sup>a</sup> Oak Ridge National Laboratory

<sup>b</sup> Argonne National Laboratory

September 20, 2019

M3CT-19OR06090121

Prepared by  
OAK RIDGE NATIONAL LABORATORY  
Oak Ridge, TN 37831-6283  
managed by  
UT-BATTELLE, LLC  
for the  
US DEPARTMENT OF ENERGY  
under contract DE-AC05-00OR22725



# CONTENTS

FIGURES .....	v
TABLES.....	vii
ABSTRACT.....	1
1. INTRODUCTION .....	1
1.1 BACKGROUND .....	1
1.2 DOCUMENT PURPOSE .....	2
1.3 APPLICATIONS .....	2
2. REVIEW OF CURRENT BUILDS.....	2
2.1 316L BUILDS.....	2
2.2 SIC BUILDS .....	4
3. 316L PRODUCED USING SLM .....	5
3.1 GENERAL APPEARANCE AND SURFACE ROUGHNESS .....	5
3.2 GENERAL MICROSTRUCTURE.....	6
3.2.1 Grain structure and orientation .....	6
3.2.2 Porosity .....	11
3.3 THERMAL PROPERTIES.....	13
3.3.1 Specific heat.....	13
3.3.2 Thermal conductivity .....	13
3.3.3 Thermal expansion.....	14
3.3.4 Thermal diffusivity .....	15
3.4 ELECTRICAL PROPERTIES.....	16
3.5 MECHANICAL PROPERTIES .....	16
3.5.1 Engineering tensile properties.....	16
3.5.2 Confirmatory tensile testing at Argonne National Laboratory .....	19
3.5.3 True stress-strain relationships .....	21
3.5.4 Elevated-temperature burst properties .....	23
3.5.5 Hardness and elastic modulus .....	26
3.5.6 Fracture/embrittlement.....	29
3.5.7 Elastic modulus, Poisson’s ratio, and shear modulus .....	29
3.5.8 Creep properties .....	29
3.5.9 Fatigue.....	34
3.5.10 Fretting and wear .....	34
4. SIC PRODUCED USING BINDERJET PRINTING AND CVI.....	35
4.1 GENERAL MATERIAL PROPERTIES AND MICROSTRUCTURE.....	35
4.2 THERMAL PROPERTIES.....	35
4.3 MECHANICAL PROPERTIES .....	36
5. CONCLUSIONS .....	38
6. REFERENCES .....	39



## FIGURES

Figure 1. Particle size distribution for SiC feedstock powder. ....	4
Figure 2. Thermogravimetry results from the aqueous binder used in binderjet printing up to 1000°C (heated at 10°C/min) in flowing argon gas (250 sccm). ....	5
Figure 3. Images showing the general appearance of components after fabrication for (a) Build 20190315 and (b) Build 20190502. ....	6
Figure 4. Typical EBSD microstructures for different objects from Build 20190308. ....	7
Figure 5. Image quality maps for the thick (massive, M) objects from Build 20190308. ....	8
Figure 6. Image quality maps for the thin (T) objects from Build 20190308. ....	9
Figure 7. EBSD maps (IPF, inverse pole figure; IQ, image quality; GROD, grain reference orientation deviation; KAM, kernel average misorientation) for the massive object of X orientation, laser 1 (M-1X). ....	9
Figure 8. Texture plots for the microstructure shown in Figure 7 (massive or thick object, laser mode 1, Build 20190308). ....	10
Figure 9. EBSD microstructures for different build geometries from Build 20190308: (a) thick plate from laser 1, (b) thick plate from laser 2, (c) thin plate from laser 2, and (d) generalized grain features based on microstructural observations. ....	11
Figure 10. Examples of types of porosity: I—keyholing, II and III—mixed keyholing and lack of fusion, IV—lack of fusion. ....	12
Figure 11. Specific heat capacity of different locations along the build height in Build 20190308 from Table 1 and mean value ( $C_{p,AM}$ , dashed line) presented. ....	13
Figure 12. Calculated thermal conductivity of AM316L from Build 20190308. ....	14
Figure 13. Mean coefficient of thermal expansion of different locations along the build height in Build 20190308 from Table 1 and mean value across the build ( $CTE$ , dashed line). ....	15
Figure 14. Thermal diffusivity of different locations along the build height in Build 20190308 from Table 1, mean value across the build ( $\alpha_{AM}$ , dashed line) and wrought values ( $\alpha_w$ , solid line) presented for comparison. ....	16
Figure 15. Tensile properties of Build 20190228 and Build 20190308 as a function of specimen orientation within the build and the test temperature: (a) yield strength, (b) ultimate tensile strength, and (c) total elongation. ....	18
Figure 16. Argonne high-temperature tensile test system. ....	19
Figure 17. Engineering stress-strain curves for AM 316L (Build 20190308) tested at 20°C. ....	20
Figure 18. Engineering stress-strain curves for AM 316L (Build 20190308) tested at 650°C. ....	20
Figure 19. Representative image of the dog-bone tensile specimen (M-1Z, i.e., massive or thick, laser 1, Z-orientation of the tensile axis), painted with white and black paint to form a random speckle pattern suitable for DIC analysis. ....	21
Figure 20. M-1Z: Four true stress–true strain curves (one from the extensometer, and three from local strain measurements, Figure 19) plotted together to demonstrate the negligible differences in the local mechanical behavior. ....	22
Figure 21. M-2X: Four true stress–true strain curves (one from the extensometer and three from local strain measurements at different locations). ....	22
Figure 22. X-ray computed tomography of the pause defect in sample 2L14 from Build 20190502. ....	24
Figure 23. Temperature and pressure profile of LOCA burst test for sample 8L12. ....	24
Figure 24. Burst temperature as a function of engineering hoop stress where (a) shows the comparison to literature values [7] and (b) shows only the values derived from this study. ....	25
Figure 25. Post-burst photographs of select specimens for nominal hoop stress of 100 MPa. ....	26
Figure 26. Scanning electron microscope image and inverse pole figure map of additively manufactured 316L after nano-indentation. ....	27

Figure 27. Elastic modulus and hardness map of additively manufactured 316L based on the results of nano-indentation study. ....	28
Figure 28. Schematic of AM 316L creep specimens (unit: in.). ....	30
Figure 29. Argonne creep test systems. ....	30
Figure 30. Creep strain as a function of time for AM 316L (Build 20190308) tested at 650°C. ....	31
Figure 31. Stress-rupture time plot for AM 316L (Build 20190308) tested at 650°C. ....	31
Figure 32. Photographs of the AM 316L (Build 20190308) creep-ruptured specimens. ....	32
Figure 33. The minimum creep rate vs. applied stress for AM 316L (Build 20190308) tested at 650°C. ....	33
Figure 34. Creep curves of AM 316L (Build 20190308) and conventional 316L tested at 650°C, 225 MPa. ....	33
Figure 35. Optical micrographs near the fracture region of the creep-tested specimens in the longitudinal direction AM 316L (top) and conventional 316L (bottom) stainless steels creep tested at 650°C, 225 MPa. ....	34
Figure 36. Optical micrograph of the cross section of binderjet printed and chemical vapor–infiltrated SiC. ....	35
Figure 37. Inverse thermal diffusivity measured on 3D printed SiC. ....	36
Figure 38. Calculated thermal conductivity of 3D printed SiC. ....	36
Figure 39. Weibull plot of SiC fracture strength from monotonic equi-biaxial flexure testing. ....	37
Figure 40. Failure probability for 3D printed SiC based on equi-biaxial flexure strength data. ....	37

## TABLES

Table 1. Summary of completed builds for 316L materials performance investigations. ....	3
Table 2. Composition of the Praxair 316L powder used in the builds summarized in Table 1.....	3
Table 3. Composition of the SiC feedstock powder within two lots from Sigma Aldrich in wt %.....	4
Table 4. Heat treatment experimental data on Build 2019-05-23.....	12
Table 5. Tensile properties of AM 316L (Build 20190308).....	20
Table 6. Cladding geometry prior to burst test. ....	23
Table 7. Measured Charpy impact properties of specimens from Build 20190308 from Table 1.....	29
Table 8. Creep test data of AM 316L (Build 20190308).....	32



## ABSTRACT

There is growing interest in the use of additive manufacturing techniques for the production and deployment of components for nuclear power applications. Specifically, the Transformational Challenge Reactor (TRC) program seeks to demonstrate the application of advanced manufacturing to rapidly develop and deploy a microreactor. As part of the TCR objective, a database on materials performance, such as thermophysical properties and mechanical performance, is required to help inform nuclear reactor designers, operators, and regulators regarding possible material limitations using emerging manufacturing techniques. The following report seeks to collect all available data regarding the material performance of candidate alloys and manufacturing processes pursued within the TCR program at Oak Ridge National Laboratory. At this time, this database focuses only on materials derived within the program and does not extend to additional manufacturing processes, manufacturers, or other advanced materials. Where appropriate, recommendations for applications of the data are provided and current knowledge gaps are identified.

## 1. INTRODUCTION

### 1.1 BACKGROUND

Increasing interest in the design and fabrication of nuclear components using additive manufacturing (AM) has developed as many AM technologies have matured to levels viable for industrial applications. These AM technologies include selective laser melting (SLM), electron beam melting, laser-directed energy deposition (L-DED), and binder jetting. They all rely on building a component layer-by-layer to form a dense component with three dimensions. SLM, which is a powder bed fusion technology, and L-DED have been targeted by the Transformational Challenge Reactor (TRC) project as viable technologies to produce core internal components using a 316L austenitic stainless steel feedstock powder. They were selected for their maturity, flexibility in control of build parameters, and current build envelopes using industry-supplied machines.

A challenge, or an opportunity, depending on how one perceives it, associated with SLM and L-DED is the selection of the appropriate process parameters to tune and tailor material properties. The processing parameters include laser power, scan speed, hatch spacing, powder layer thickness, scanning/build strategy, atmosphere, and powder bed temperature. A single adjustment of a single parameter can have strong effects on the final component's material performance parameters, including strength (e.g., yield strength), ductility, fracture resistance, porosity, surface finish, and thermophysical properties. Moreover, layer-wise fabrication leads to additional complexity: different layers in a complex component can see varying time-temperature profiles over the variation of the build, leading to localized variances in material performance parameters. The complex linkage between process parameters and local heating profiles means an increased possibility of scatter in the materials performance parameters compared with components/specimens fabricated using traditional ingot metallurgy.

The larger predicted scatter band in materials performance for 316L using either SLM or L-DED thus needs to be characterized and documented to enable proper reactor design and performance predictions, even in low-power (<20 MW thermal) systems such as those currently being investigated within TCR.

Binder jet 3D printing is another unique technology that is performed at near room temperature and therefore it is highly agnostic to the feedstock powder. It presents the opportunity to additively build nuclear-grade ceramics into complex green body structures. These green bodies subsequently need to be densified. The densification is often carried out by secondary phase melt infiltration or sintering. Secondary phase infiltration is problematic for environments with irradiation resulting in displacement

damage (i.e., nuclear reactor cores), as they tend to degrade two-phase materials, which respond differently to irradiation. Sintering, on the other hand, results in shrinkage and often damage in complex 3D structures. A novel methodology<sup>1</sup> for the production of carbide ceramics was developed recently and is being leveraged to produce ceramic inert fuel matrix or structures for the TCR core [1].

In this report, an effort is made to develop and report a database on materials properties and performance parameters for additively manufactured 316L components derived using either SLM or L-DED processes, as well as 3D printed nuclear-grade SiC produced at the Manufacturing Demonstration Facility (MDF) at Oak Ridge National Laboratory (ORNL). This handbook draws on a half-year of intensive research on AM materials processing and performance for TCR. As it is the first edition, no effort was made to include data produced outside MDF, primarily because the validity of the data would have to be extensively verified to ensure its applicability to the design of any TCR-derived reactor. It is intended that this edition will be updated as more results and data are generated over the coming fiscal years within the TCR effort.

## **1.2 DOCUMENT PURPOSE**

This document is the first effort to quantify the available physical, mechanical, thermal, and performance properties data for candidate additively-manufactured materials to produce the core structures of the TCR, including 316L and SiC. When available, trends or variations based on the generalized location within a single build (print), and/or batch-to-batch variability, are identified to enable the user to identify and design for the inherent variability of AM approaches. This handbook is intended for use by researchers, modelers, and reactor designers.

## **1.3 APPLICATIONS**

This document is primarily intended to inform the design community for the TCR of the performance of candidate materials and manufacturing processes. It can also be used for future reactor designs or implementation where the materials and manufacturing processes presented within are of interest.

# **2. REVIEW OF CURRENT BUILDS**

## **2.1 316L BUILDS**

The current builds completed on 316L feedstock are summarized in Table 1. For the remainder of the document, the Build ID is correlated to the data presented. Table 1 shows that only components fabricated using the SLM powder bed fusion process have been investigated to date, with the powder feedstock and processing parameters held constant across all builds. The Concept Laser-M2 has the added benefit of using two identical laser systems on different sections/regions of the powder bed to fabricate larger components. This two-laser system enables direct one-to-one batch variability within a single build while holding all other variables constant.

All builds in Table 1 used the same powder feedstock with the nominal composition provided in Table 2.

---

<sup>1</sup> US Patent Application No. 16/527,317

**Table 1. Summary of completed builds for 316L materials performance investigations.**

<b>Build ID</b>	<b>Machine</b>	<b>AM Tech</b>	<b>Powder manufacturer</b>	<b>Composition</b>	<b>Parameters</b>	<b>Post-processing</b>	<b>Geometries</b>	<b>Goal</b>
20190228	Concept Laser – M2	SLM	Praxair	316L	Vendor recommended	None	Round bar, thick plate, thin plate	Provide baseline materials data
20190308	Concept Laser – M2	SLM	Praxair	316L	Vendor recommended	None	Round bar, thick plate, thin plate, hex “flower,” hex tube	Provide baseline materials data
20190315	Concept Laser – M2	SLM	Praxair	316L	Vendor recommended	None	Round bar, thick plate, hex “flower”	Provide baseline in situ data
20190502	Concept Laser – M2	SLM	Praxair	316L	Vendor recommended	None	Thin-walled tubes	Provide tube burst data, unsuccessful
20190507	Concept Laser – M2	SLM	Praxair	316L	Vendor recommended	None	Thin-walled tubes	Provide tube burst data, unsuccessful
20190508	Concept Laser – M2	SLM	Praxair	316L	Vendor recommended	None	Thin-walled tubes	Provide tube burst data, successful
20190523	Concept Laser – M2	SLM	Praxair	316L	Vendor recommended	See Section 3.2.2, Porosity	ASTM tensile test specimens	Provide heat treatment data, ongoing

3

**Table 2. Composition of the Praxair 316L powder used in the builds summarized in Table 1.**

<b>Fe</b>	<b>Cr</b>	<b>Ni</b>	<b>Mo</b>	<b>Mn</b>	<b>Si</b>	<b>N</b>	<b>Cu</b>	<b>Co</b>	<b>C</b>	<b>P</b>	<b>O</b>
Bal.	17.07	12.08	2.41	1.19	0.46	0.01	0.01	0.1	0.006	<0.005	0.05

## 2.2 SIC BUILDS

The properties for the SiC materials described in this report are for those derived from  $\alpha$ -SiC (hexagonal phase) feedstock powder with a  $\sim 20\ \mu\text{m}$  diameter (Figure 1) from Sigma Aldrich with a purity  $>99.5\%$ . Table 3 shows the detailed chemical composition of the feedstock powder (Luvak Inc., Boylston, MA) determined via direct current plasma emission spectroscopy and combustion infrared detection (according to ASTM E 1097-12 and ASTM E 1019-18, respectively). The Innovent binderjet printing system from ExOne Company (North Huntingdon, PA) was used for the production of test specimens. An aqueous binder (Binder 05 from ExOne) was used during printing; it underwent curing at  $190^\circ\text{C}$  for 6 h in air. The curing step drives off the majority of the aqueous binder, and during the next step of the process, the high temperatures almost completely drive it off. Figure 2 shows the weight evolution of the aqueous binder and upon heating in argon to a high temperature, implying that it is almost entirely decomposed and dissociated away from the part at temperatures above  $500^\circ\text{C}$ .

After a green part is binderjet printed and cured, it is transferred to the chemical vapor infiltration (CVI) furnace, where it undergoes densification. The furnace decomposes a mixture of hydrogen with methyltrichlorosilane gases at  $\sim 1000^\circ\text{C}$  to deposit high-purity, stoichiometric, and crystalline SiC around the 3D printed SiC powder particles. To control the SiC deposition rate and achieve optimal infiltration, an isobaric pressure on the order of 200 torr is maintained inside the furnace. Depending on the size of the part, the CVI process may take hours to days to close all the open porosity in the part.

**Table 3. Composition of the SiC feedstock powder within two lots from Sigma Aldrich in wt %. No other elements detected in excess of 0.01 wt % (100 wppm).**

Lot#	Si/C ratio	Si	C	Al	Fe	V	Zr
MKCF-9014	1.024	70.9	29.6	0.025	–	–	0.017
MKCJ-4732	1.006	70.1	29.8	0.019	0.04	0.016	0.017

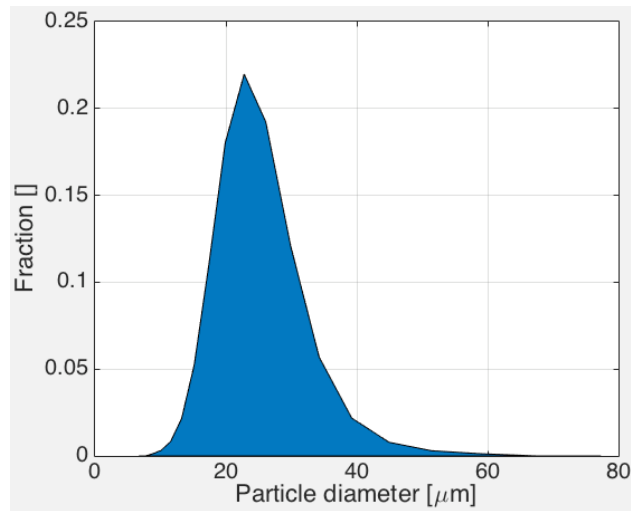


**Figure 1. Particle size distribution for SiC feedstock powder.**

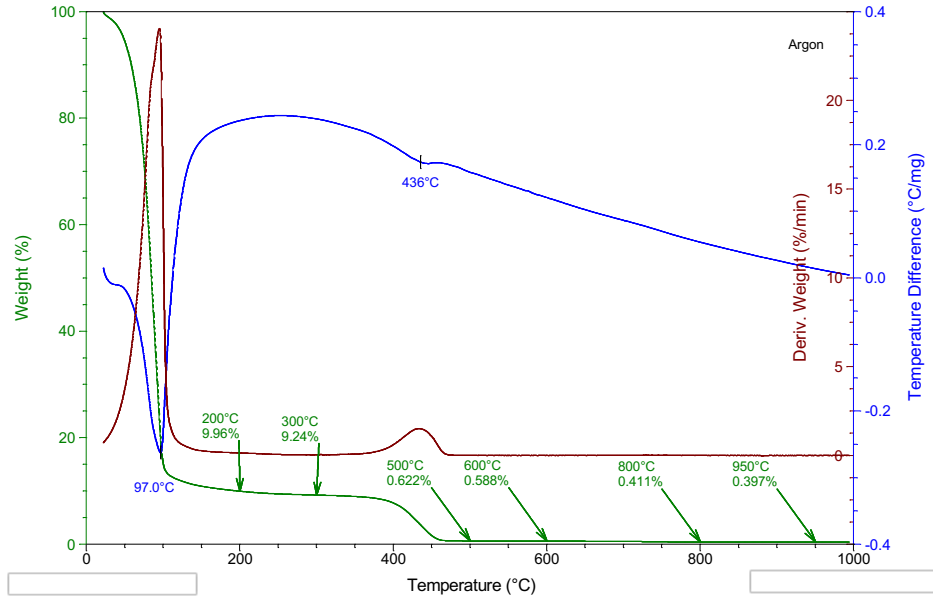


**Figure 2. Thermogravimetry results from the aqueous binder used in binderjet printing up to 1000°C (heated at 10°C/min) in flowing argon gas (250 sccm).**

### 3. 316L PRODUCED USING SLM

#### 3.1 GENERAL APPEARANCE AND SURFACE ROUGHNESS

Optical photographs were taken after each build to show the general appearance; examples of the images are shown in Figure 3. For certain builds and component geometries, visually apparent flaws can be detected. These flaws were typically associated with complex geometries or areas of significant overhang—such as the walled structures seen in Figure 3b, or were directly associated within known faults/errors in the build—such as the restart during Build 20190502, which lead to a noticeable line defect in the tube components. Overall, the frequency of visual defects was limited, and most components appear structurally sound and free of macro-size defects on external surfaces.

All builds showed an apparent surface morphology that was quantified using a stylus probe for the thick plate component in Build 20190308. The measurement was made using a stylus drag both parallel and perpendicular to the build direction; the average roughness was quantified as  $R_a=6.0\pm 0.4 \mu\text{m}$  and no difference was observed resulting from component fabrication on different lasers in the M2 system or build position.

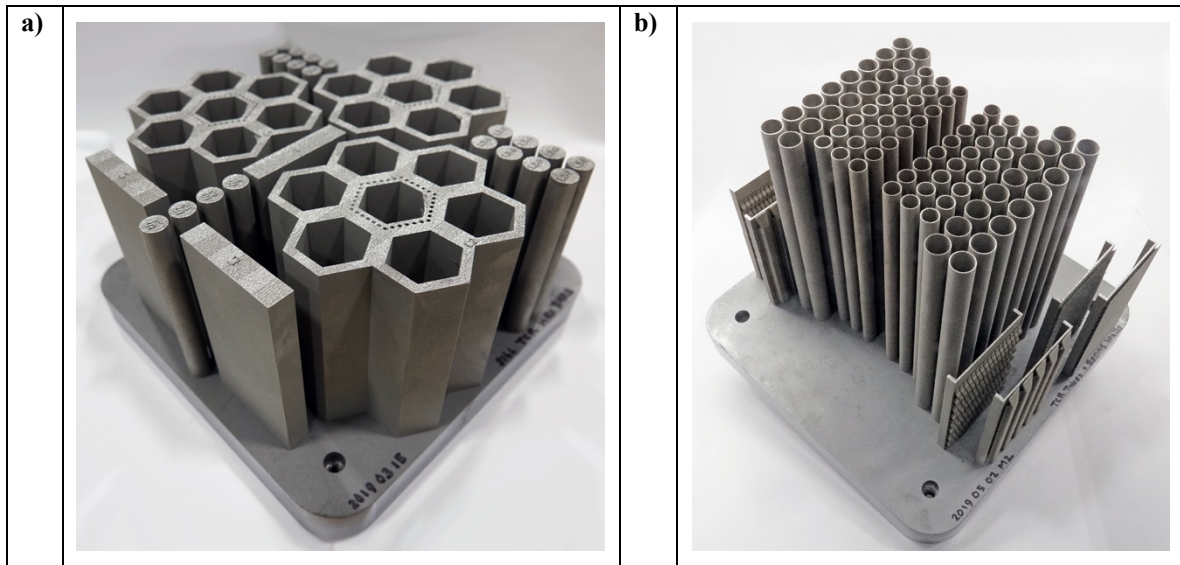


**Figure 3. Images showing the general appearance of components after fabrication for (a) Build 20190315 and (b) Build 20190502.**

### **3.2 GENERAL MICROSTRUCTURE**

Specimens for microstructure analysis were cut from the prescribed locations of Build 20190308; the specimen set included thick (or “massive”) and thin objects built using both laser modes (i.e., laser 1 and laser 2). The specimens were epoxy mounted and prepared using standard metallography procedures with colloidal silica as a final preparation step. Electron backscatter diffraction (EBSD) analysis was performed at a Tescan scanning electron microscopy (SEM) equipped with an Oxford Symmetry EBSD detector.

#### **3.2.1 Grain structure and orientation**

Figure 4 shows representative images of the grain microstructures of the studied objects. It is apparent that the microstructure in all cases is distinctly different from that of a common annealed or cold-worked material. The grains are much smaller than in annealed austenite and, in most cases, have an elongated shape. The typical microstructural element is a group (i.e., cluster) of elongated or bent grains forming specific crescent-shaped formations. These formations are thought to be the remnants of the welding pools, many of which were remelted and partially or fully destroyed by subsequent laser beam passes. Groups of much smaller grains often exist between the crescent-shaped formations.

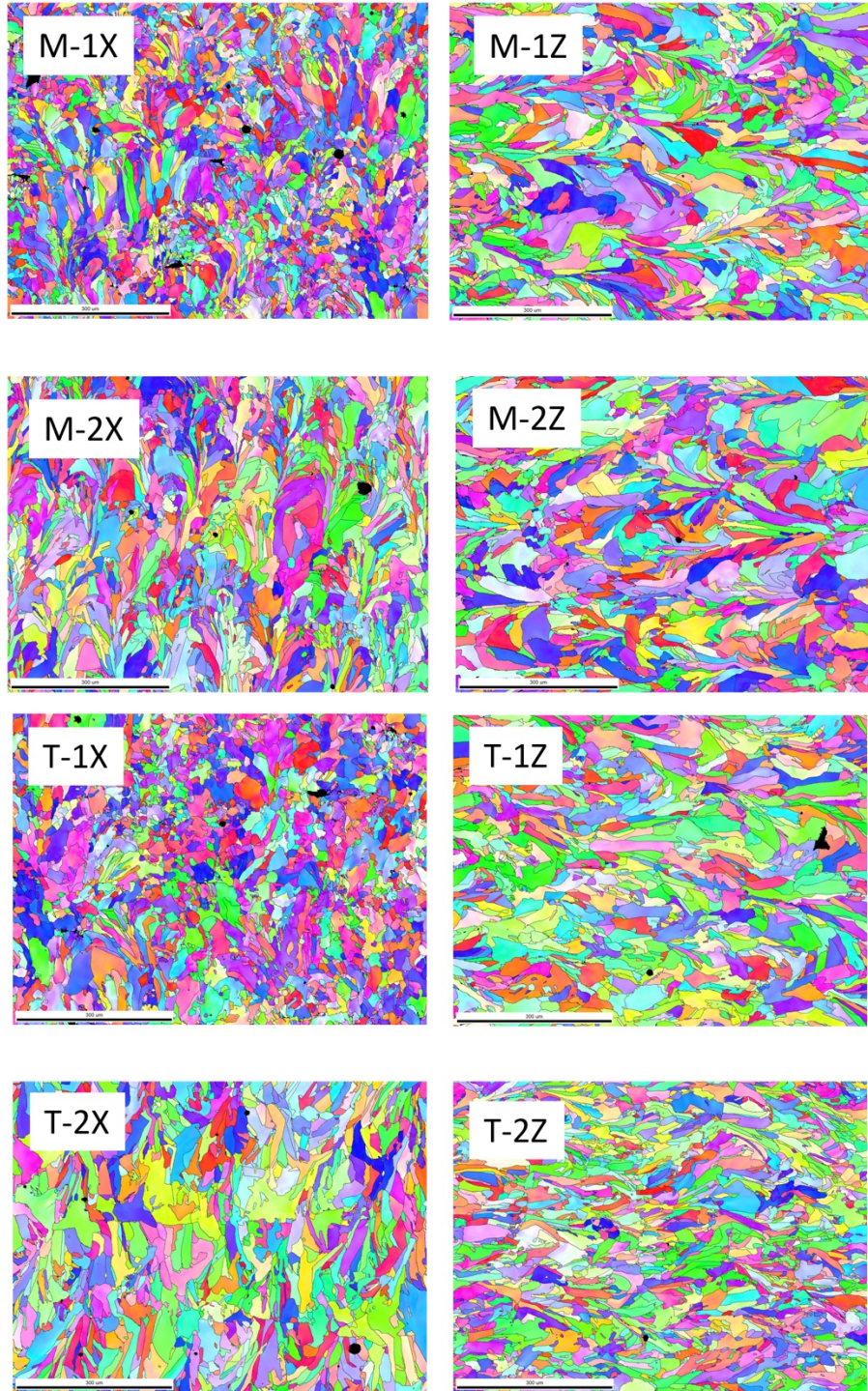


**Figure 4. Typical EBSD microstructures for different objects from Build 20190308.** “M” designates massive (or thick) plate and “T” designates thin plate. A 1 or 2 corresponds to the laser 1 and laser 2 modes, respectively. For each condition, two orientations (X and Z) were analyzed. Length scales are identical for all images. Inverse pole figures are colored in the tensile direction (which is horizontal for all maps).

Figure 5 shows image-quality (IQ) or Kikuchi diffraction pattern–quality maps for the massive objects and Figure 6 shows the same maps for thin objects. The IQ maps accurately represent grain morphology; reveal deformation bands and signs of twinning and phase transformation, if any; and show defects in

structure (e.g., pores, delamination). It can be seen that pores and specific elongated defects are present in most images, but their density in all cases is below  $\sim 1\%$ .

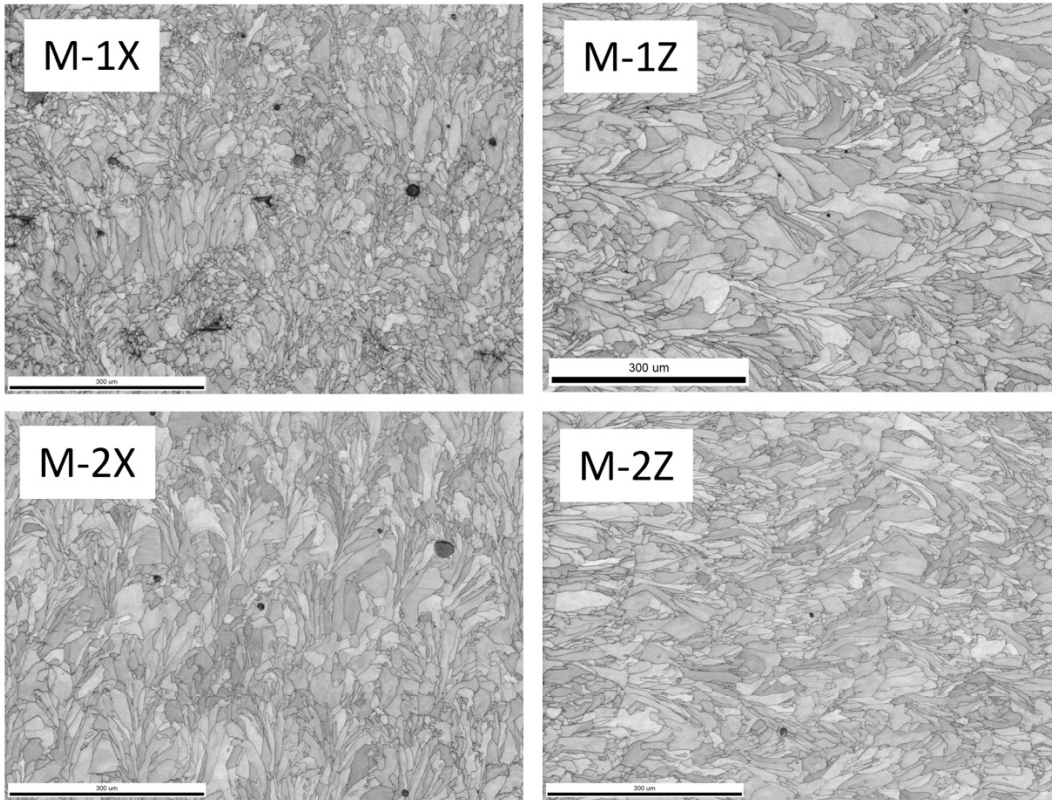
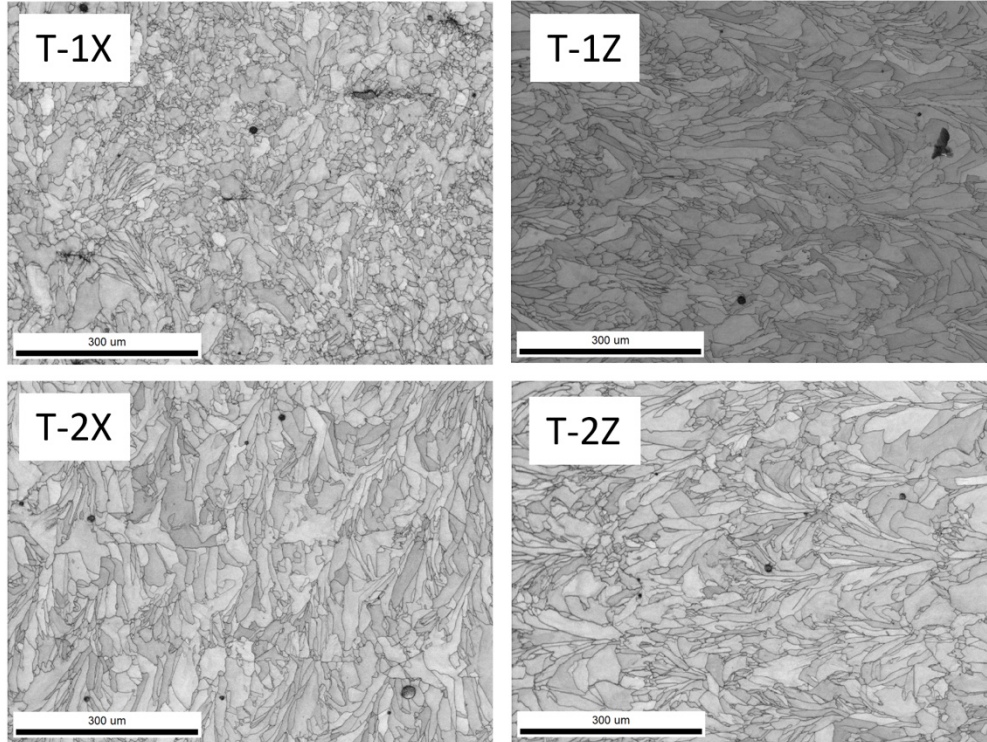


**Figure 5. Image quality maps for the thick (massive, M) objects from Build 20190308.** Designation nomenclature is the same as in Figure 4.

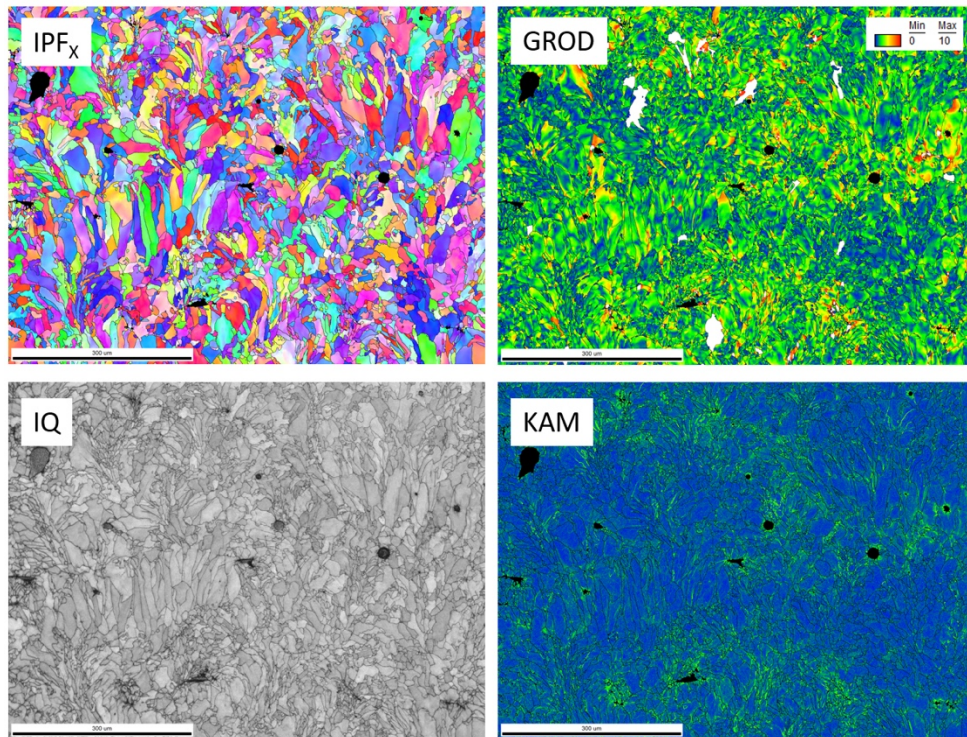
Figure 7 shows an extended EBSD data set for a massive object. In addition to the inverse pole figure (IPF) and IQ maps, GROD (grain reference orientation deviation) and KAM (kernel average misorientation) maps are shown to highlight the misorientation in the structure.

Thus, the GROD map, showing lattice bending and rotation within a single grain, demonstrates misorientation values up to  $\sim 10^\circ$ . The map suggests that the material experienced some plastic strain, roughly equivalent to  $\sim 4\text{--}8\%$  of tensile deformation at room temperature. The KAM map shows strong variations across the map: low-KAM areas interlace with high-KAM spots. The high-KAM spots form specific clusters (i.e., groups of grains with elevated KAM), suggesting a layered structure with  $150\text{--}200\ \mu\text{m}$  steps between the spots. One may speculate that plastic strain was caused by cooling and contraction of material volumes surrounding the welding pools. Therefore, it appears that pool overlapping and multiple passes formed a microstructure with pronounced GROD and KAM inhomogeneity.

Similar nonuniform misorientation distributions (not included in the present report) were observed for all analyzed conditions (i.e., massive *and* thin objects, laser modes 1 *and* 2) and directions.

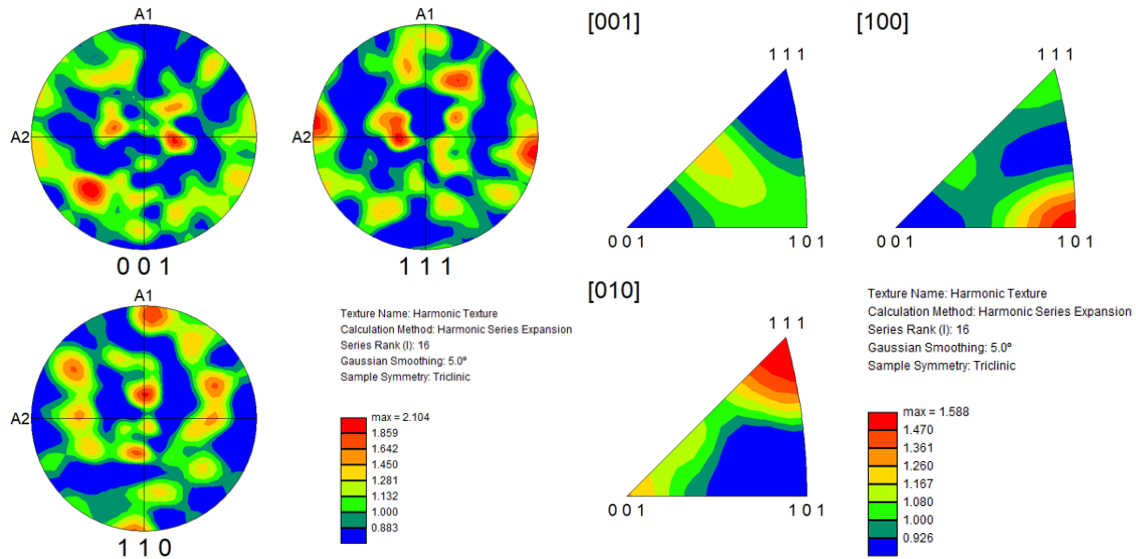


**Figure 6. Image quality maps for the thin (T) objects from Build 20190308. Designation nomenclature is the same as in Figure 4.**



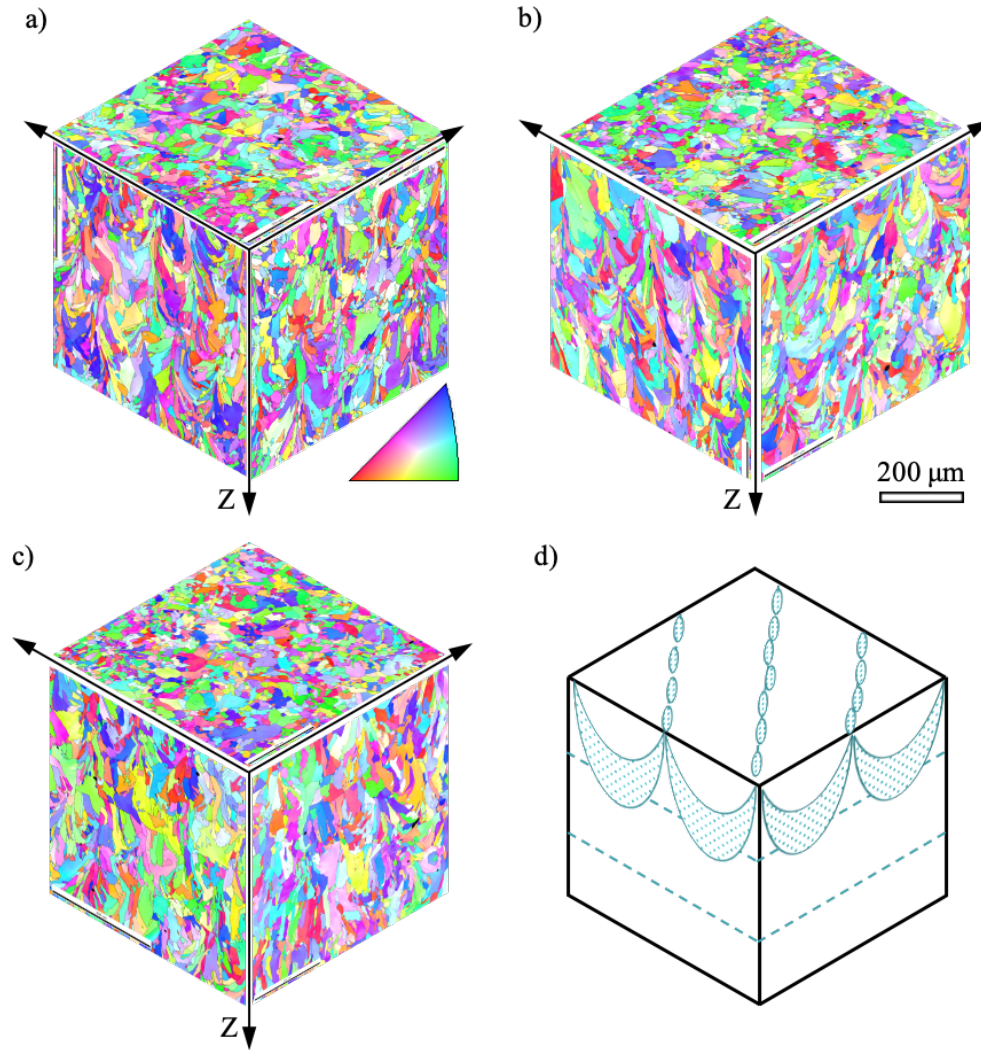
**Figure 7. EBSD maps (IPF, inverse pole figure; IQ, image quality; GROD, grain reference orientation deviation; KAM, kernel average misorientation) for the massive object of X orientation, laser 1 (M-1X). For objects from Build 20190308. Length scales are identical for all images.**

Figure 8 shows typical texture plots for additively manufactured 316L steel. Whereas some specific texture components are present in the data, texturing, in general is very weak (only  $\sim 1.6\text{--}2 \times$  random). Such values may be routinely observed in annealed stainless steel plates available on the market. Maximums in the IPF plots suggest slightly elevated fractions of some specific grain families (e.g.,  $[101]$ -oriented grains in the  $[100]$ -map), but those features are expected to have negligible consequences regarding mechanical behavior and material performance.



**Figure 8. Texture plots for the microstructure shown in Figure 7 (massive or thick object, laser mode 1, Build 20190308). Left: Pole figure plots. Right: the same data represented as IPF plots.**

Figure 9 provides a summary of the studied conditions; the microstructure was observed for all three planes (i.e., cross-sections). It is apparent that an ordered microstructure is always present in the maps in the Z-direction, which is the build direction. The ordered structure is thought to reflect multiple laser beam passes and partial overlapping of the welding pools. Further data analysis is in progress.



**Figure 9. EBSD microstructures for different build geometries from Build 20190308: (a) thick plate from laser 1, (b) thick plate from laser 2, (c) thin plate from laser 2, and (d) generalized grain features based on microstructural observations. Length and color scale is identical for all images.**

### 3.2.2 Porosity

Porosity is known in the literature to be related to at least two distinct phenomena—lack of fusion and keyholing. Lack of fusion occurs when insufficient energy is applied to the melt pool to completely melt the powder bed, resulting in the type of porous structure seen in Figure 10 III and IV. Keyholing occurs when too much energy is applied to a melt pool and localized vaporization of molten material occurs. The pockets of vaporized metal are unable to travel to the surface of the melt pool and collapse before the melt pool solidifies; as a result, pores remain in the solidified material. Lack-of-fusion porosity is characterized by irregular pores or even the outlines of unmelted or partially melted powder, whereas keyholing porosity is characterized by spherical relatively dimensionally uniform pores.

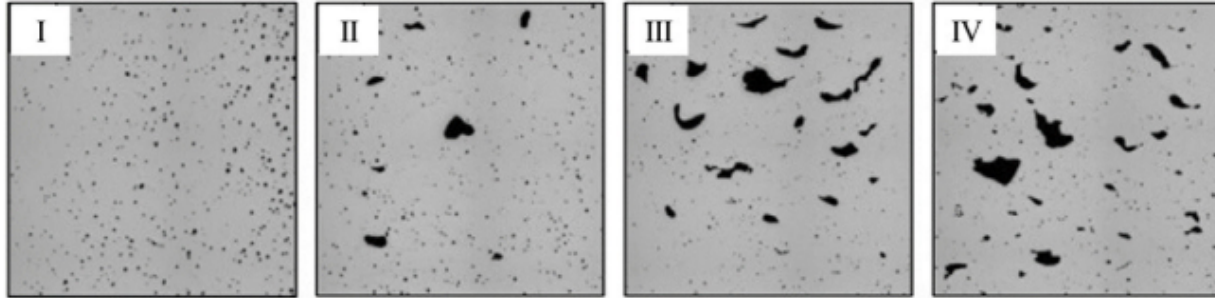


**Figure 10. Examples of types of porosity: I—keyholing, II and III—mixed keyholing and lack of fusion, IV—lack of fusion. Source: DebRoy et al. 2018 [2]**

Experimental porosity data are available from a heat treatment study conducted for additively manufactured 316L on a Concept Laser M2. In that study, a set of experiments with five tests were conducted, as indicated in Table 4. Group 2 was the ideal heat treatment based on the literature, and groups 1 and 3 were references to determine the effects of hot isostatic pressing (HIP) and furnace cooling, respectively. HIP is expected to reduce porosity and improve mechanical properties, and furnace cooling is more likely to precipitate carbides at grain boundaries. Groups 4 and 5 were stress-relieving heat treatments; while these heat treatments were not expected to transform residual ferrite to austenite, they were expected to relieve stress without forming grain boundary carbides. Four samples were fabricated on each laser for each test group with the default concept laser parameters, for a total of eight samples per test group. Samples were sealed in quartz tubes under partial pressure argon (0.25 atm, 99.999% purity) and heat-treated in the same furnace (CM Furnaces model 1730-20HT, serial 180592), with the exception of group 1. All samples were heated at 10°C/min. Group 1 was rapidly quenched within the HIP machine, and all other groups were quenched by placing the hot quartz tubes on a large steel heat sink plate and air cooling them. All samples were obtained from Build 2019-05-23.

Optical images at 5× multiplication were obtained for one sample from each test group, converted to black and white masks, and analyzed for porosity with ImageJ. Pores on the edges of images were included in porosity percentage measurements. Porosity measurements are listed in Table 4. Tests were performed between laser 1 and laser 2 for each heat treatment group; there was no statistically significant difference in porosity between the two lasers for any heat treatment group (P Value 5%). As of the time of this report (September 20, 2019) the heat-treated specimens are undergoing machining and tensile testing according to ASTM E8.

**Table 4. Heat treatment experimental data on Build 2019-05-23.**

Group	Temperature (°C)	Time (min)	Pressure (MPa)	Cooling	Sample ID	Mean porosity	STDEV	99.9th percentile
1	1100	60	100	Quench	L1-01	0.022%	0.011%	0.055%
					L2-01	0.012%	0.005%	0.026%
2	1100	60	0	Quench	L1-05	0.135%	0.051%	0.293%
					L2-05	0.119%	0.020%	0.182%
3	1100	60	0	10°C/min	L1-09	0.158%	0.025%	0.237%
					L2-09	0.149%	0.020%	0.258%
4	650	30	0	Quench	L1-13	0.142%	0.021%	0.208%
					L2-13	0.139%	0.022%	0.208%
5	650	30	0	10°C/min	L1-17	0.117%	0.013%	0.156%
					L2-17	0.126%	0.031%	0.222%

L1 = laser 1; L2 = laser 2.

A design of experiments for various machine combinations of power, velocity, spot size, and hatch spacing has been designed and is expected to be run in late September 2019, or when the build queue permits. The measured dependent variables are porosity, upskin surface roughness, downskin surface roughness, melt pool depth, melt pool width, and qualitative scoring of feature resolution.

### 3.3 THERMAL PROPERTIES

A series of thermal properties studies have been completed on Build 20190308 to establish the baseline thermal properties of the additively produced 316L alloys compared with variants produced using traditional ingot metallurgy.

#### 3.3.1 Specific heat

The specific heat of Build 20190308 has been measured using a Netzsch differential scanning calorimeter (DSC) 404 C. Samples were heated at 20 K/min<sup>-1</sup> followed by cooling to room temperature at 20 K/min<sup>-1</sup>. The cooling curves are shown as a function of build height (top, middle, and bottom) in Figure 11. The specific heat capacity did not have a strong variation based on build height; hence the mean value for the build can be approximated using a simple linear relationship:

$$c_p = b + m \cdot T, \quad (1)$$

where  $c_p$  is the specific heat capacity (J kg<sup>-1</sup>K<sup>-1</sup>),  $b$  and  $m$  are fitting constants,  $T$  is the temperature in K. In the case of Build 20190308, the fitting constants were found to be 0.425 J kg<sup>-1</sup>K<sup>-1</sup> and 1.673×10<sup>-4</sup> J kg<sup>-1</sup>K<sup>-2</sup> for  $b$  and  $m$ , respectively. These values correlated closely with those proposed by Kim for wrought 316L [3], as shown in Figure 11.

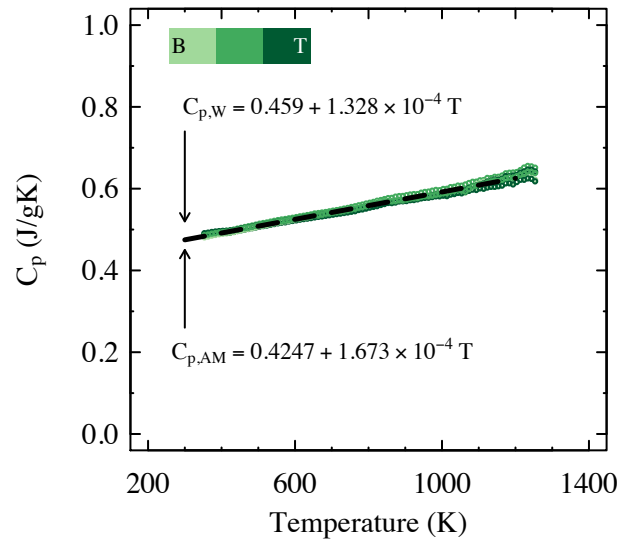


**Figure 11. Specific heat capacity of different locations along the build height in Build 20190308 from Table 1 and mean value ( $C_{p,AM}$ , dashed line) presented. Wrought values ( $C_{p,w}$ , solid line) presented for comparison. Color bar shows location in build: B for bottom and T for top.**

#### 3.3.2 Thermal conductivity

The thermal conductivity ( $\kappa$ ) of the Build 20190308 alloys was calculated using Eq. (2):

$$\kappa = \alpha c_p d , \quad (2)$$

where  $\alpha$  is the thermal diffusivity,  $c_p$  is the specific heat capacity,  $d$  is the specimen density. The density was estimated assuming 99% density of the wrought value reported by Kim [3] at room temperature. This value remained constant across the temperature range investigated. The values over the temperature range for  $\alpha$  and  $c_p$  were extracted from Figure 14 (presented on page 16) and Figure 11, respectively, for the AM values (subscripted “AM”). The resulting estimation and comparison with the relationship provided by Kim [3] is shown in Figure 12. Figure 12 shows reasonable alignment between the wrought values and Build 20190308 up to 600 K. The deviation between the two data sets above 600 K is most likely not compensating for decreasing density at elevated temperatures in Build 20190308. The values could be further refined, but that has not been done to date.

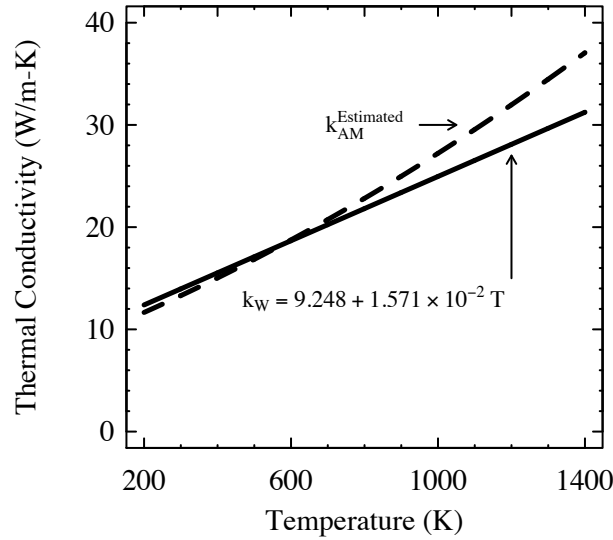


**Figure 12. Calculated thermal conductivity of AM316L from Build 20190308.**

### 3.3.3 Thermal expansion

The thermal expansion coefficient was measured for Build 20190308 across the build height of the specimens using a Theta Deal push-rod thermal expansion system with a heating rate of 3°C/min in ultra-high purity (UHP) helium. Minimal variation was found among the samples extracted at different locations with the data provided in Figure 13, with the dashed line representing the mean value based on the application of a four order polynomial:

$$CTE = A_1 T^4 + A_2 T^3 + A_3 T^2 + A_4 T + A_5 , \quad (3)$$

where  $A_{1-5}$  are fitting constants and  $T$  is the temperature in K. The constants are provided in the text of Figure 13.

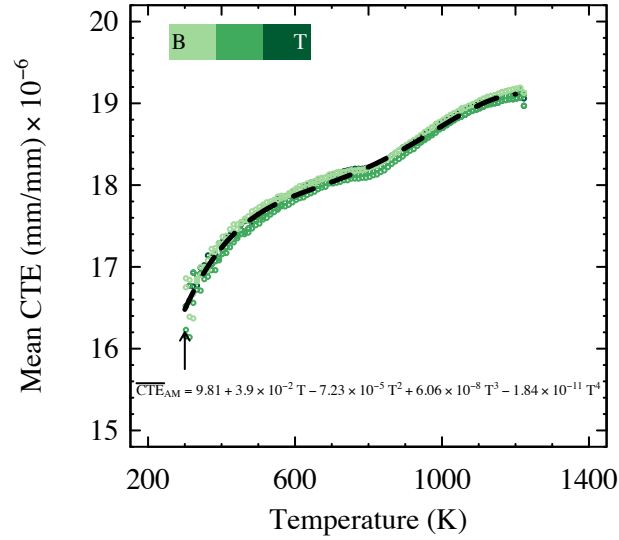


**Figure 13. Mean coefficient of thermal expansion of different locations along the build height in Build 20190308 from Table 1 and mean value across the build ( $\overline{CTE}$ , dashed line). Color bar shows location in build: B for bottom and T for top.**

### 3.3.4 Thermal diffusivity

The thermal diffusivity was measured using a Netzsch LFA 457 flash diffusivity instrument, with the results presented in Figure 14. Samples were extracted at various build heights to determine if any variation in the thermal diffusivity; Figure 14 indicates no significant variation. The mean value was determined by fitting the individual data points to a second order polynomial:

$$\alpha = A_1 T^2 + A_2 T + A_3 , \quad (4)$$

where  $A_{1-3}$  are fitting constants and  $T$  is the temperature in K. The constants are provided in the text of Figure 14. These values correlated closely with those proposed by Kim for wrought 316L [3], as shown as the solid line in Figure 14.

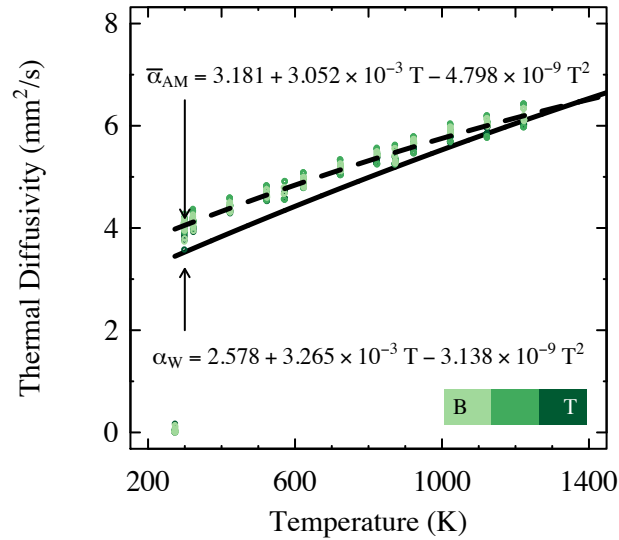


**Figure 14. Thermal diffusivity of different locations along the build height in Build 20190308 from Table 1, mean value across the build ( $\bar{\alpha}_{AM}$ , dashed line) and wrought values ( $\alpha_w$ , solid line) presented for comparison. Color bar shows location in build: B for bottom and T for top.**

### 3.4 ELECTRICAL PROPERTIES

The electrical properties of ORNL-derived 316L have not been studied to date.

### 3.5 MECHANICAL PROPERTIES

#### 3.5.1 Engineering tensile properties

The tensile properties of Build 20190228 and Build 20190308 have been investigated for a series of specimen geometries, build locations, and test conditions. The tensile sample geometries include ASTM sub-sized round bar geometry (gage 31.75 mm  $\times$  6.35 $\phi$  mm) using threaded grips, as well as the less common but well-established SS-J3 sub-sized specimen geometry (gage: 5  $\times$  1.75  $\times$  0.75 mm). The SS-J3 specimen geometry was selected, as its diminutive size enables extracting samples from multiple height locations and orientations within a single build, it has been demonstrated to reasonably approximate larger ASTM standard geometries in austenitic stainless steels [4], and it is widely used in irradiations within the High Flux Isotope Reactor, thus providing baseline data for future irradiation studies. All samples were tested using a strain rate of approximately  $10^{-3} \text{ s}^{-1}$ ; SS-J3 specimens were tested in the shoulder loading condition. Figure 15 summarizes the resulting tensile properties from Build 20190228 and Build 20190308. As a comparison, the EN10028 standard for 316L stainless steels as described in the ITER materials handbook [5] and the ASME minimum requirement for ingot metallurgy produced 316 are included in Figure 15.

Figure 15 shows several distinct trends. First, the tensile properties follow the common reduction in strength with increasing test temperature with the elevated temperature testing ( $>100^\circ\text{C}$ ) falling on or near the ASME minimum requirement for ultimate tensile strength. Scatter in the strength parameters is also apparent in Figure 15 but has not been quantified to date. Note that some scatter is expected based on variance in test geometries and variances in compliances intrinsic across the multiple load frames used. Interestingly, the ductility also decreased with increasing test temperature; the mechanisms for such a loss are still under investigation. Variances in the strength and ductility depending on the orientation of the extracted tensile geometry were also observed in the Z-direction (gage aligned parallel to the build

direction), showing higher strength compared with the X-direction (gage aligned perpendicular to the build direction). At room temperature, the Z-direction shows consistently lower ductility, but this observation is reversed between the two directions in elevated-temperature testing. The variance in performance at elevated temperature could be an increased dependency on the intrinsic porosity induced during the manufacturing process.

The results in Figure 15 show that the yield strength of ORNL-derived heats of 316L exceed the international standards across the temperature range specified. The ultimate tensile strength is at or above acceptable levels at room-temperature ambient testing; but at elevated temperatures, the values cannot meet the ASME minimum requirement. Further investigation is needed to determine the root cause of the decreased ultimate tensile strength compared with the traditionally manufactured variants used in standards testing.

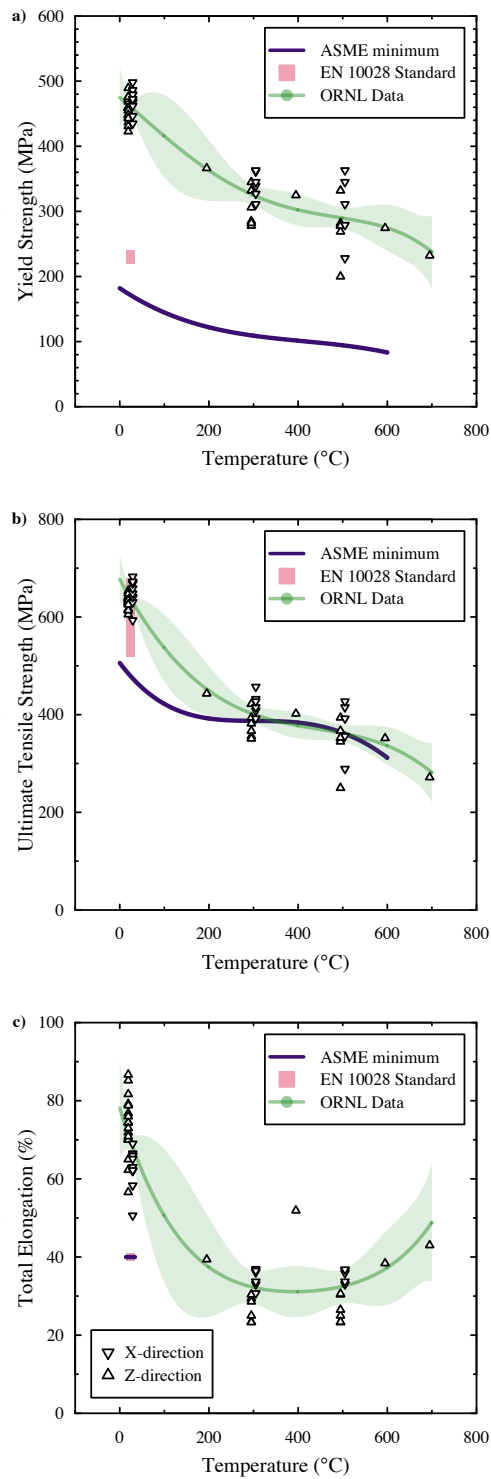


**Figure 15. Tensile properties of Build 20190228 and Build 20190308 as a function of specimen orientation within the build and the test temperature: (a) yield strength, (b) ultimate tensile strength, and (c) total elongation.**

### 3.5.2 Confirmatory tensile testing at Argonne National Laboratory

Confirmatory tensile testing was carried out at Argonne National Laboratory (Argonne). The tests were conducted on two lots of tensile specimens fabricated from Build 20190308 from laser 1 (specimen ID: L1TX) and laser 2 (specimen IDs: L1TX) modes. The SS-J3 sheet-type specimens were made from the upper right regions of thick plate sections (massive 1Z for laser 1; massive 2Z for laser 2).

Figure 16 shows a setup for high-temperature tensile tests at Argonne. Tensile tests were performed in an electromechanical testing system equipped with Instron Bluehill software. Tensile tests were conducted at 20 and 650°C at a nominal strain rate of  $1 \times 10^{-3}$ /s using a set of shoulder-loading grips. The applied load was recorded by a load cell; the specimen displacement was measured by the crosshead extension. The engineering tensile properties were determined from the analysis of the load and displacement data.



**Figure 16. Argonne high-temperature tensile test system.**

The room-temperature engineering stress-strain curves for specimens of laser 1 and laser 2 modes are shown in Figure 17. A portion of the stress-strain curves are nearly identical up to ~40% for laser 1 and laser 2 specimens. The major difference is the uniform elongation where necking occurred (48.4% for the laser 1 specimen and 62.5% for the laser 2 specimen). Figure 18 shows the engineering stress-strain curves for AM316L Build 20190308 tested at 650°C. The laser 1 specimen has a lower yield stress and uniform and total elongations than the laser 2 specimen. Both curves show serrations after the yield, indicating a dynamic strain aging effect (DSA) in AM 316L. The DSA effect is slightly stronger in the laser 2 specimen than in the laser 1 specimen. The tensile properties, i.e., yield stress, ultimate tensile strength, and uniform and total elongations, are summarized in Table 5.

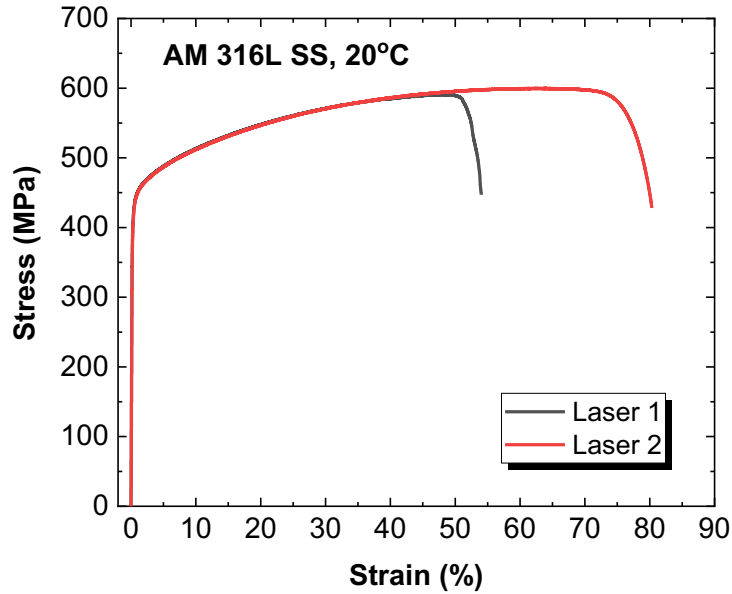


Figure 17. Engineering stress-strain curves for AM 316L (Build 20190308) tested at 20°C.

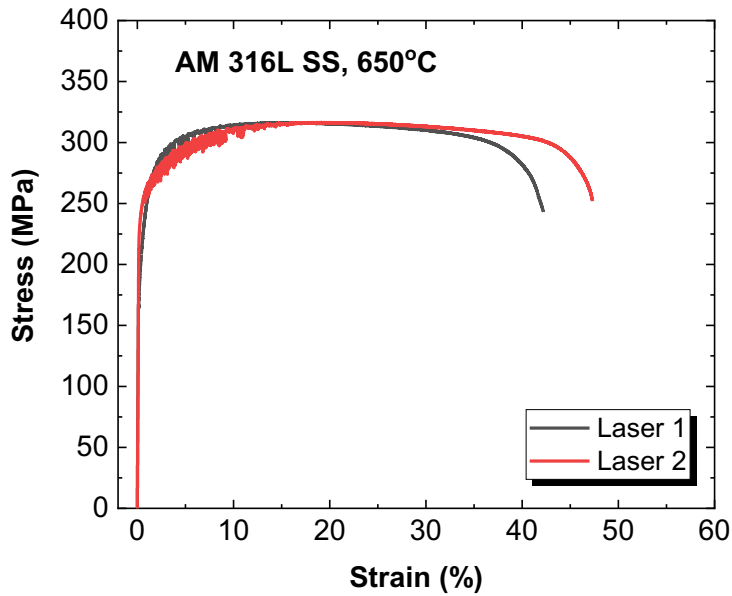


Figure 18. Engineering stress-strain curves for AM 316L (Build 20190308) tested at 650°C.

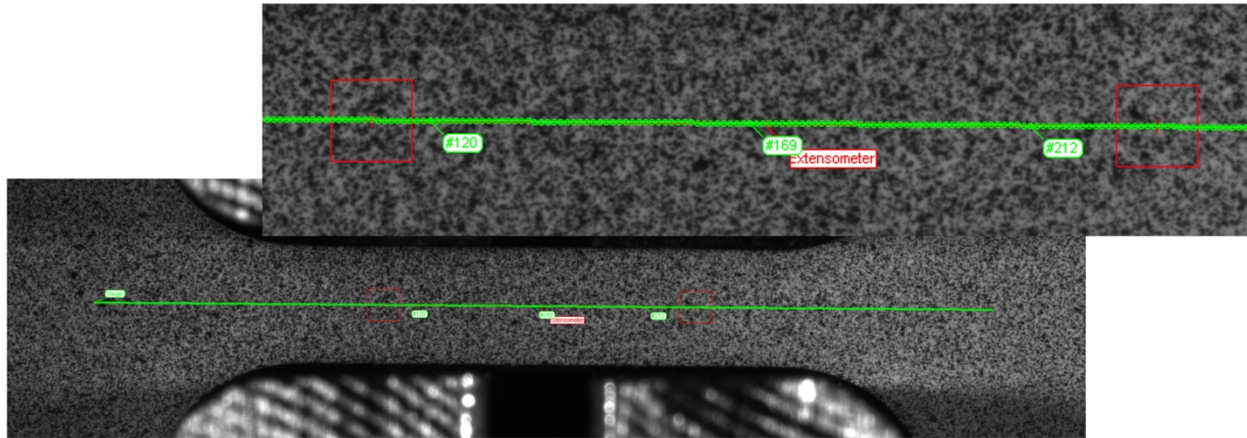
Table 5. Tensile properties of AM 316L (Build 20190308).

Sample ID	AM condition	Test T (°C)	YS (MPa)	UTS (MPa)	UE (%)	TE (%)
L1T1	Laser 1	20	422	591	48.4	54.2
L2T1	Laser 2	20	414	599	62.5	80.5
L1T2	Laser 1	650	198	316	15.5	42.7
L2T2	Laser 2	650	241	316	19.2	47.5

### 3.5.3 True stress-strain relationships

Tensile testing at room temperature was accompanied by noncontact strain measurements via digital image correlation (DIC) analysis. DIC is now a common research tool that allows for collecting valuable information on strain localization, appearance and propagation of deformation bands, necking peculiarities, and material behavior on a local scale. Because AM produces parts and components layer by layer, there might be concerns regarding material and property homogeneity. One could expect that local mechanical behavior might vary to some degree from layer to layer because of the variation in grain morphology, local preexisting misorientation, pores, and other factors.

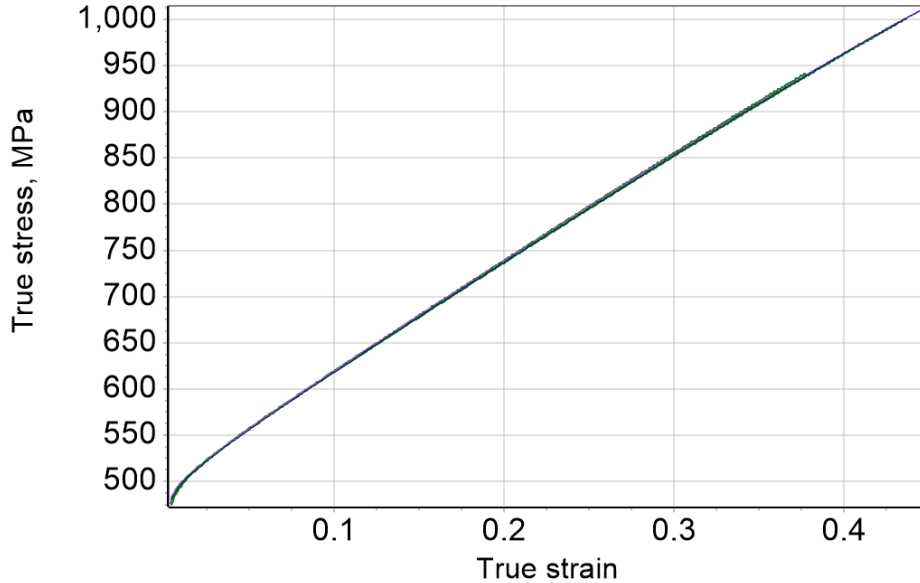
Tensile tests were performed on an MTS Insight 2-52 one-column tensile screw machine. Before the testing, the specimens were painted with white and black paint, forming a random speckle pattern (Figure 19). A single Allied Vision GX3300 digital camera was employed to capture images during the tests; the resolution was  $\sim 5 \mu\text{m}$  per pixel. The camera frame rate was 16 frames per second, but only one image per second was stored for the analysis. Two-dimensional strain fields were calculated using VIC-2D commercial software and a homemade program using common DIC algorithms. True stress–true strain curves were calculated using common constant volume criteria, with the assumption that material density changes during straining are negligible.



**Figure 19. Representative image of the dog-bone tensile specimen (M-1Z, i.e., massive or thick, laser 1, Z-orientation of the tensile axis), painted with white and black paint to form a random speckle pattern suitable for DIC analysis. A magnified image at the top shows pattern quality and density. Strain distribution was analyzed along the tensile axis (green line, representing digital object introduced by DIC software) and for the middle portion of the specimen gauge (red object labeled “extensometer”).**

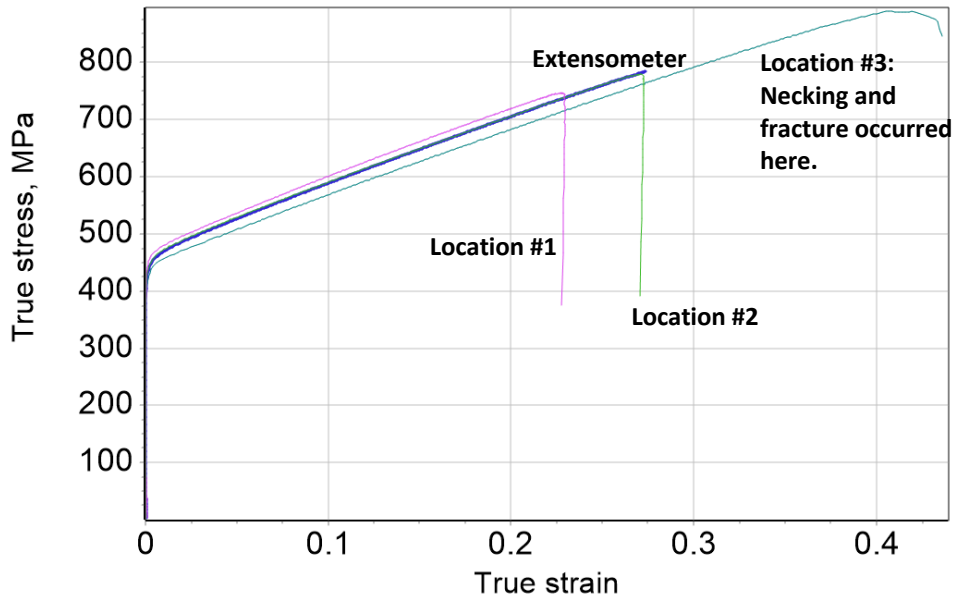
To evaluate the true stress–true strain curves, two approaches were employed. First, a digital extensometer was located in the middle portion of the specimen (i.e., the red object in Figure 19). The extensometer evaluated the average mechanical behavior for the selected specimen volume. Second, local strains were evaluated along the specimen tensile axis (i.e., the green object in Figure 19) with a step of five pixels; a few points (3–4: left gauge portion, middle of the gauge, right portion) were selected for further analysis.

Figure 20 shows four true stress–true strain curves for different areas along the specimen gauge. Plotted together, the curves are practically identical; the random error was small enough, and local mechanical behavior along the Z-direction (i.e., the tensile axis of the specimen) experienced very weak, if any, variations for this particular specimen.



**Figure 20. M-1Z: Four true stress–true strain curves (one from the extensometer, and three from local strain measurements, Figure 19) plotted together to demonstrate the negligible differences in the local mechanical behavior.**

Figure 21 shows another case: observable variations in the local hardening behavior. It can be seen that at the same true strain value, the true stress may vary by up to ~4–5% or slightly more. The variations may be caused by flaws or defects such as voids in the microstructure. This case represents the largest variability observed at the moment.



**Figure 21. M-2X: Four true stress–true strain curves (one from the extensometer and three from local strain measurements at different locations).**

From a physics-of-plasticity point of view, the true stress–true strain curves have close-to-parabolic shapes typical of dislocation-controlled deformation mechanisms. Small strain areas (below ~0.05) and

large strain areas (0.05 or more) may have slightly different strain hardening rates, depending on the number of active slip systems per grain and other factors. Detailed analysis is in progress.

### 3.5.4 Elevated-temperature burst properties

The burst properties were determined from Build 20190502 and Build 20190508 using the integral loss of coolant accident (LOCA) furnace module in the Severe Accident Test Station [6]. In brief, tube specimens of varying outer and inner dimensions were fabricated and then sectioned from the base plate. Tubes were then fitted with matching zirconia rods inside the tubes, and Swaglok fittings were used to provide a leaktight fitting interface to the LOCA furnace module. The LOCA furnace module heated each tube individually using an 8 kW infrared furnace at 5°C/s. All tubes were ~150 mm long and internally pressurized. The tube geometries prior to burst testing are provided in Table 6. Test tubes included both those with visible defects due to a build stop associated with Build 20190502, and those with no visual defects from Build 20190508. An example of the extent of the defects in tubes from Build 20190502 is shown in the series of images in Figure 22.

**Table 6. Cladding geometry prior to burst test.**

Build #	Label	Laser(s)	OD (mm)	Wall thickness (mm)	Defect
2019 05 02 M2	2L11	1	12.7	0.508	Pause/Offset
2019 05 02 M2	2L12	1	12.7	0.381	Pause/Offset
2019 05 02 M2	2L13	1	9.525	0.508	Pause/Offset
2019 05 02 M2	2L14	1	9.525	0.381	Pause/Offset
2019 05 02 M2	2L15	1	9.525	0.254	Pause/Offset
2019 05 02 M2	2L21 <sup>†</sup>	2	12.7	0.508	Pause/Offset
2019 05 02 M2	2L22	2	12.7	0.381	Pause/Offset
2019 05 02 M2	2L23 <sup>†</sup>	2	9.525	0.508	Pause/Offset
2019 05 02 M2	2L24	2	9.525	0.381	Pause/Offset
2019 05 02 M2	2L25	2	9.525	0.254	Pause/Offset
2019 05 08 M2	8L11	1	12.7	0.508	None
2019 05 08 M2	8L12	1	12.7	0.381	None
2019 05 08 M2	8L13	1	9.525	0.508	None
2019 05 08 M2	8L14	1	9.525	0.381	None
2019 05 08 M2	8L15	1	9.525	0.254	None
2019 05 08 M2	8L21	2	12.7	0.508	None
2019 05 08 M2	8L22	2	12.7	0.381	None
2019 05 08 M2	8L23	2	9.525	0.508	None
2019 05 08 M2	8L24	2	9.525	0.381	None
2019 05 08 M2	8L25	2	9.525	0.254	None

Wall thinning and increased porosity were observed for all specimens with the pause-generated defect, with the severity of the defect varying based on location on the build plate. During heat loading, temperature was monitored using three Type-S thermocouples. Burst was monitored using a miniature pressure transducer affixed to the test configuration. The burst test sequence consisted of heating the internally pressurized tube in flowing argon to 100°C, followed by a 120 s hold, and then heating to 300°C, followed by a 300 s hold. The purpose of both holds was to check the test assembly for pressure leaks. After proper sealing was ensured, the test assembly was heated at 5°C/s to a maximum temperature of 1200°C. The pressure was monitored for a significant drop (signaling tube burst), at which point temperature ramp was immediately ended and the entire testing configuration was air quenched. The

pressure and temperature prior to the significant drop were taken as the burst pressure and burst temperature, respectively. The LOCA temperature and pressure profile for sample 8L12 is shown in Figure 23, with the heating/holding sequences and burst temperature/pressure labeled.

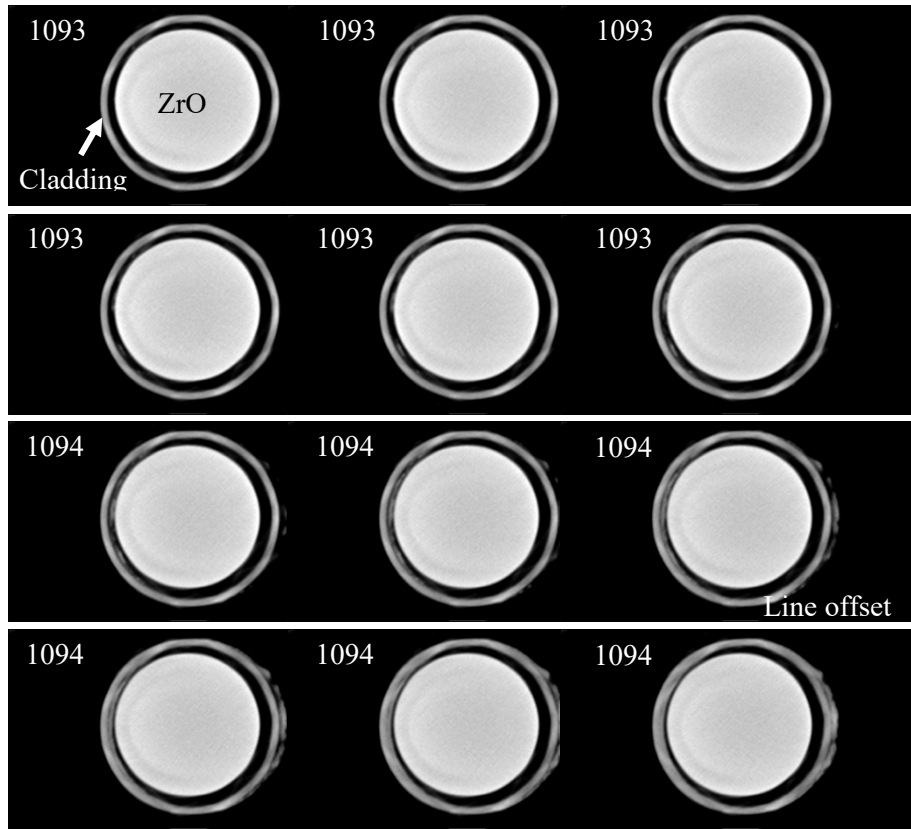


Figure 22. X-ray computed tomography of the pause defect in sample 2L14 from Build 20190502.

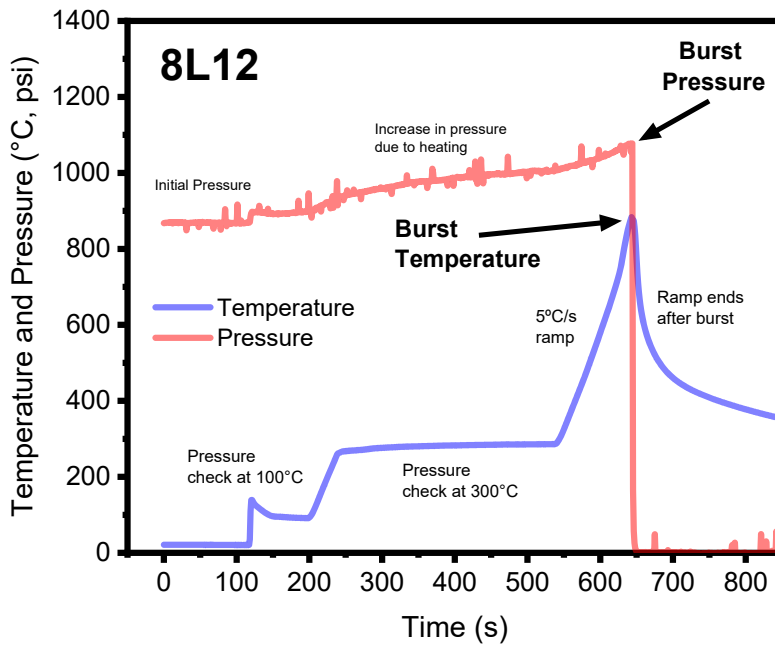


Figure 23. Temperature and pressure profile of LOCA burst test for sample 8L12.

The true hoop stress ( $\sigma_0$ ) was nominally held constant across the test matrix in Table 6 by altering the internal pressure using the relationship

$$\sigma_0 = \Delta p \frac{r}{w}, \quad (5)$$

where  $\Delta p$  is the internal rod pressure,  $r$  is the cladding mid-radius, and  $w$  is the thickness. Owing to the inert conditions of the testing configuration, it was assumed that  $r$  and  $w$  were independent of time and temperature.

The results from the tube bursts are shown in Figure 24. Results from Yamada, which were produced from tubes manufactured using traditional processes, are included for comparison [7]. The results of the additively produced tubes show general agreement with the burst temperatures observed for conventionally manufactured tubes in the range of 100–200 MPa hoop stress. Surprisingly, no significant variation in burst temperature was found for tubes with known defects versus those without. Similarly, no strong correlation was observed for tubes manufactured using either laser within the M2 system (Figure 24b). These initial burst results indicate that a similar performance in thin-walled structures could exist between traditionally manufactured 316L components and those components manufactured on the M2 system.

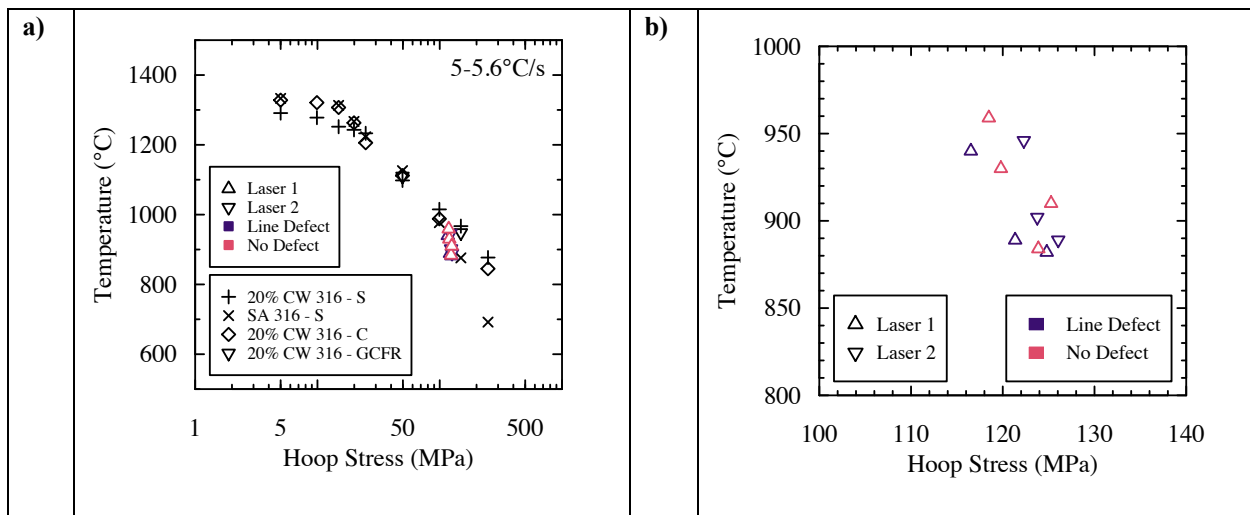


**Figure 24. Burst temperature as a function of engineering hoop stress where (a) shows the comparison to literature values [7] and (b) shows only the values derived from this study.**

Figure 25 shows the post-burst photography of the various tested specimens from Table 6 and Figure 24. Note that the zirconia rods can be observed in the internals of the burst location. The general configuration showed limited ballooning with burst openings generally being the same morphology and size across all specimens tested. The general morphology implied that rapid plastic deformation occurred immediately before tube burst, which is consistent with the results for other iron-based alloys, such as those in the study conducted by Massey et al. [8]. For specimens that contained a known pause-induced defect, the burst opening was seen to correspond with the location of the defect, even though the defect was not axially centered during the test. This result indicates that a defected region before it bursts is the weakest location in the tubes.

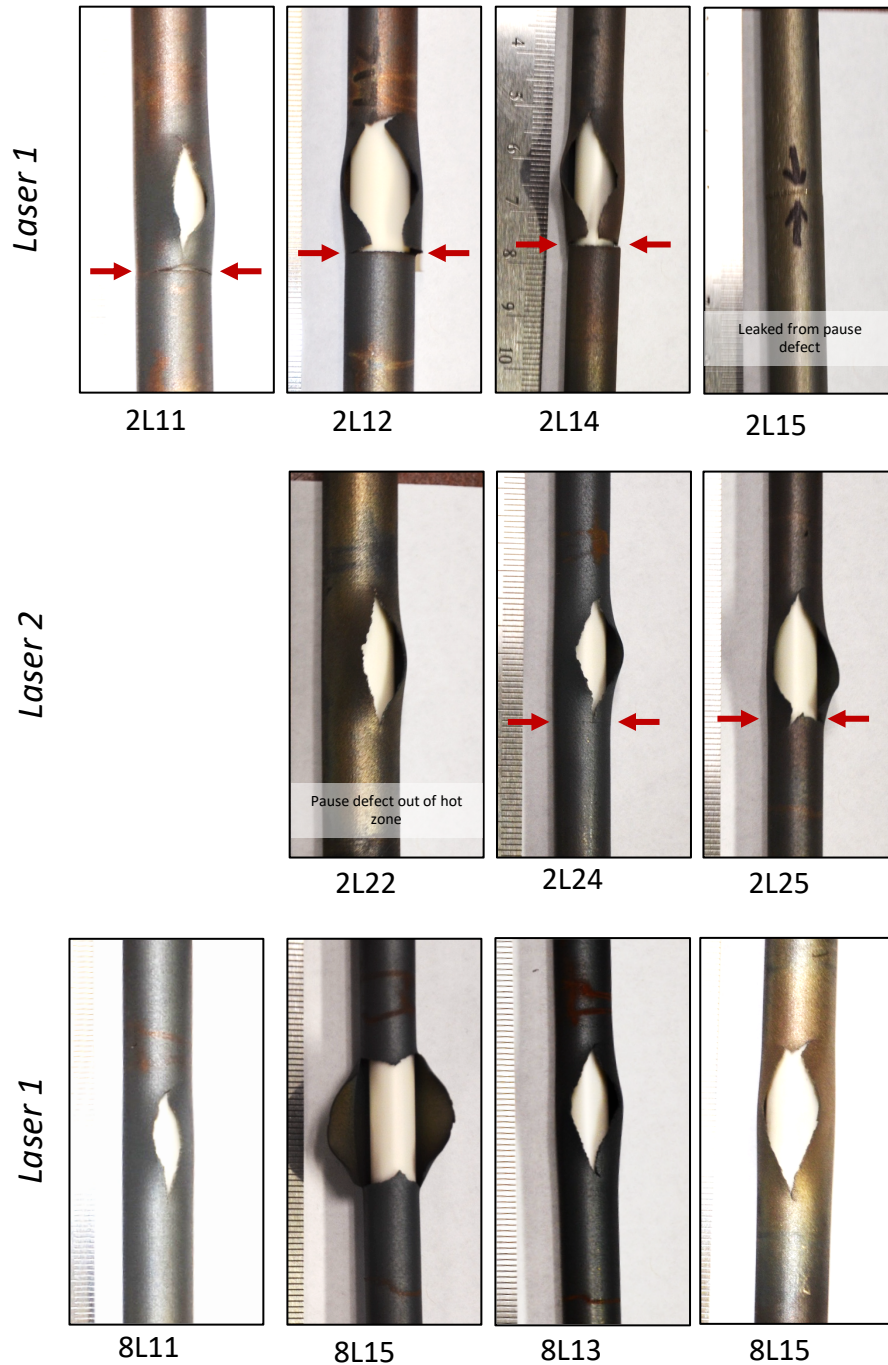


Figure 25. Post-burst photographs of select specimens for nominal hoop stress of 100 MPa.

### 3.5.5 Hardness and elastic modulus

The mechanical properties mapping was obtained by a generated grid of individual nano-indentation patterns made on the 316L specimens in Build 20190228 using a Hysitron 900 nanoindenter. An indenter tip of known geometry (e.g., Berkovich tip) was projected into specific sites—in this case, at each grid node in the material. An increasing load was then applied and when it reached the designated maximum value, unloading was performed until the load was removed. The slope of unloading close to the

maximum load represented the stiffness which, along with plastic deformation depths was used to calculate the elastic modulus and hardness of material at the site.

In the present work, we made 900 indentions into a  $30 \times 30$  grid with a maximum load of  $5000 \mu\text{N}$ , with a mean depth of indentation of  $265 \text{ nm}$  on SS-316L (AM-massive 1X). The indentation spacing was maintained at  $\sim 2 \mu\text{m}$ . The area of the indentation grid was then analyzed in a Tescan SEM by performing EBSD to correlate the mechanical properties with the crystal structure (Figure 26). The determined values for elastic modulus and hardness were mapped and plotted in Figure 27 as contour plots over the area of the study.

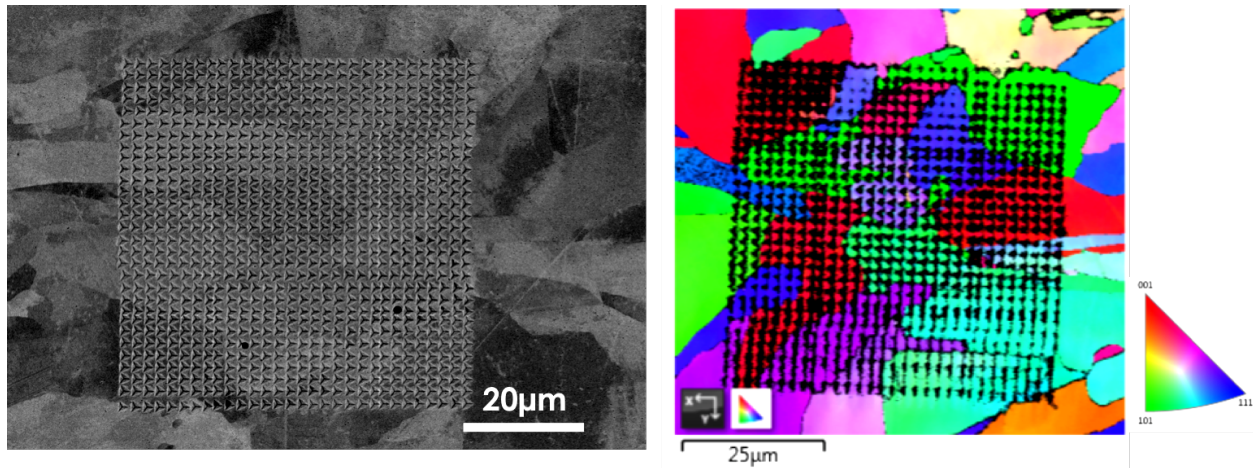


**Figure 26. Scanning electron microscope image and inverse pole figure map of additively manufactured 316L after nano-indentation.**

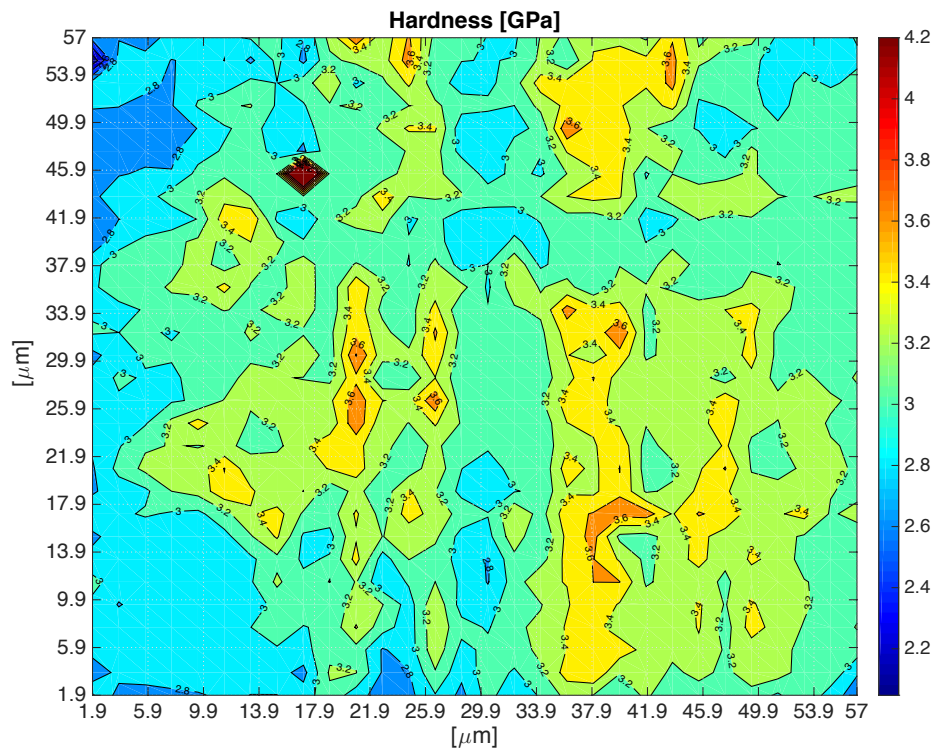
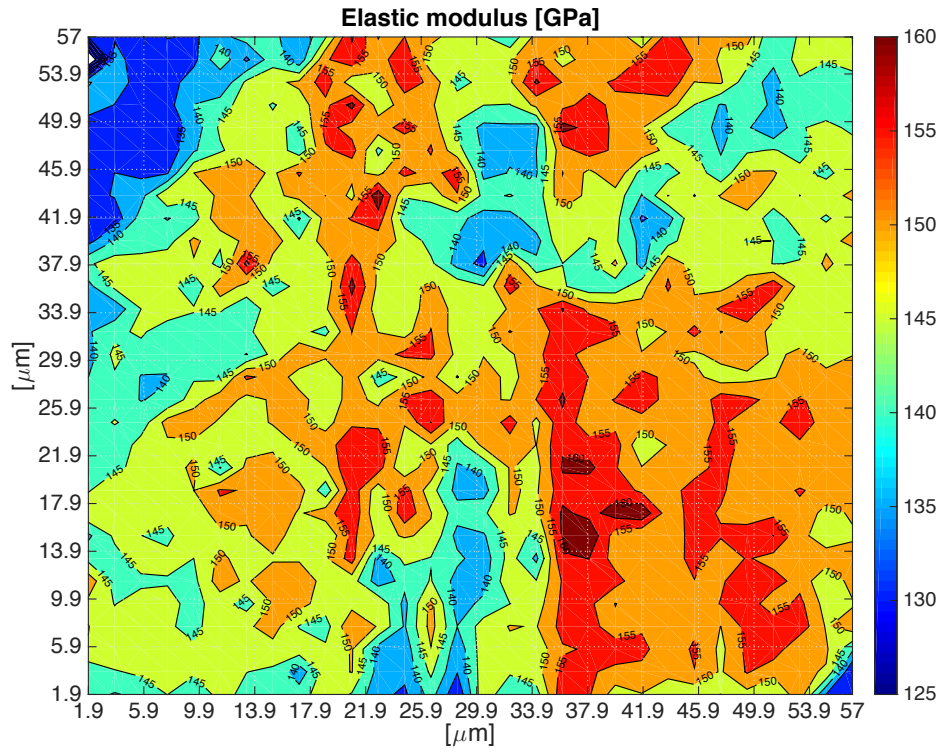


**Figure 27. Elastic modulus and hardness map of additively manufactured 316L based on the results of nano-indentation study.**

### 3.5.6 Fracture/embrittlement

The fracture properties of Build 20190308 were studied at different height locations using ½ size ASTM Charpy V-notch specimens. The notch was orientated to be both parallel (X) and perpendicular (Z) to the build direction in the specimen. All tests were performed at room temperature. The results of the testing are provided in Table 7. The results show no significant difference in the absorbed impact energy and fracture mechanism across the build height regardless of the orientation of the specimens. All samples exhibited 100% shear after testing. Note that the testing was completed using ½ size specimens, and hence a direct correlation of the results cannot be made with common standards such as EN 10028-7. However, ½ size specimen results are useful for screening Charpy properties of materials machined from different builds, locations, or orientations.

**Table 7. Measured Charpy impact properties of specimens from Build 20190308 from Table 1.**

Laser	Geometry	Orientation	Spec	Energy (J)	% Shear
1	Top	X	TX1	21.7	100
1	Middle	X	MX1	25.8	100
1	Bottom	X	BX1	24.4	100
1	Top	Z	TB1	24.4	100
1	Middle	Z	MB1	23.4	100
1	Bottom	Z	BB1	21.7	100
2	Top	X	TX2	25.8	100
2	Middle	X	MX2	24.4	100
2	Bottom	X	BX2	26.4	100
2	Top	Z	TB1	29.5	100
2	Middle	Z	MB2	30.5	100
2	Bottom	Z	BB2	24.4	100

### 3.5.7 Elastic modulus, Poisson’s ratio, and shear modulus

Aside from the indentation study in Section 3.5.4, the elastic modulus, Poisson’s ratio, and shear modulus of ORNL-derived 316L have not been studied to date and will be determined in the future using resonance ultrasonic spectroscopy (RUS).

### 3.5.8 Creep properties

ASTM-standard round bar specimens were fabricated from Build 20190308 of additively manufactured 316L stainless steel. The specimen drawing is given in Figure 28. Two lots of creep specimens were sent from ORNL to Argonne for creep testing. The first lot of three specimens were made from round bar sections of laser 1 mode (specimen ID, L1XX), and the second lot of three specimens were made from round bar sections of laser 2 mode (specimen ID, L2XX).

Creep tests were conducted according to the ASTM Standard E139-11, “Standard Test Methods for Conducting Creep, Creep-Rupture, and Stress-Rupture Tests on Metallic Materials.” Creep tests were carried out on the ATS Series 2300 Lever Arm Creep Testing Systems integrated with WinCCS II computer control and data acquisition software package (Figure 29). Each creep machine is equipped with a three-zone split-tube furnace capable of operation at up to 1100°C. Three creep specimens of laser

1 mode were tested at 650°C in air at stress levels of 175, 200, and 225 MPa, respectively. Three specimens of laser 2 mode were tested under the same conditions.

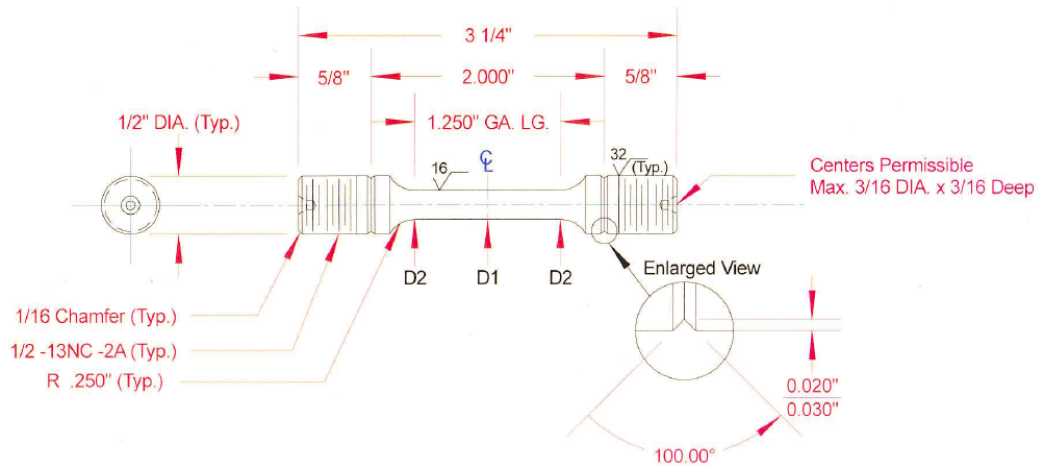


**Figure 28. Schematic of AM 316L creep specimens (unit: in.).**



**Figure 29. Argonne creep test systems.**

Figure 30 shows the creep strain as a function of time for the six creep specimens. Figure 31 plots the stress against the rupture time on a log-log scale. The photographs of the six creep-ruptured specimens are shown in Figure 32, indicating that fracture occurs near the center of the gauge section in most of the specimens. Note that specimens made from laser 1 and laser 2 modes showed remarkably comparable creep behavior. The only major difference is the creep rupture strains of the specimens tested at 200 MPa (40.7% for laser 1 and 53.5% for laser 2). No steady-state creep was observed in any of the six tests. The minimum creep strain rate was reached in the first few hours, followed by a continuous increase to failure. The minimum creep strain rate was measured and is reported in Table 8. Table 8 also lists the rupture time, creep rupture strain, and reduction of area. The creep rupture strain and the reduction of area were measured using the two fractured parts of each specimen.

Figure 33 shows the minimum creep rate as a function of the applied stress on a log-log scale for AM 316L (Build 20190308). No obvious differences can be observed between specimens made from laser 1

and laser 2 modes. The creep rate follows a power law relationship with the applied stress,  $\dot{\epsilon} = A\sigma^n$  with the power exponent of  $n = 12$ , which implies a low-temperature dislocation creep mechanism.

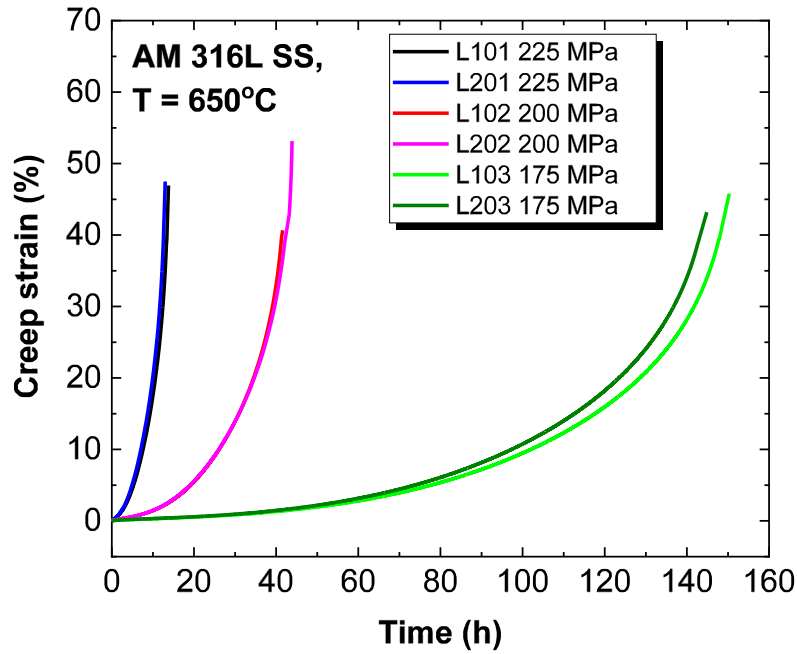


Figure 30. Creep strain as a function of time for AM 316L (Build 20190308) tested at 650°C.

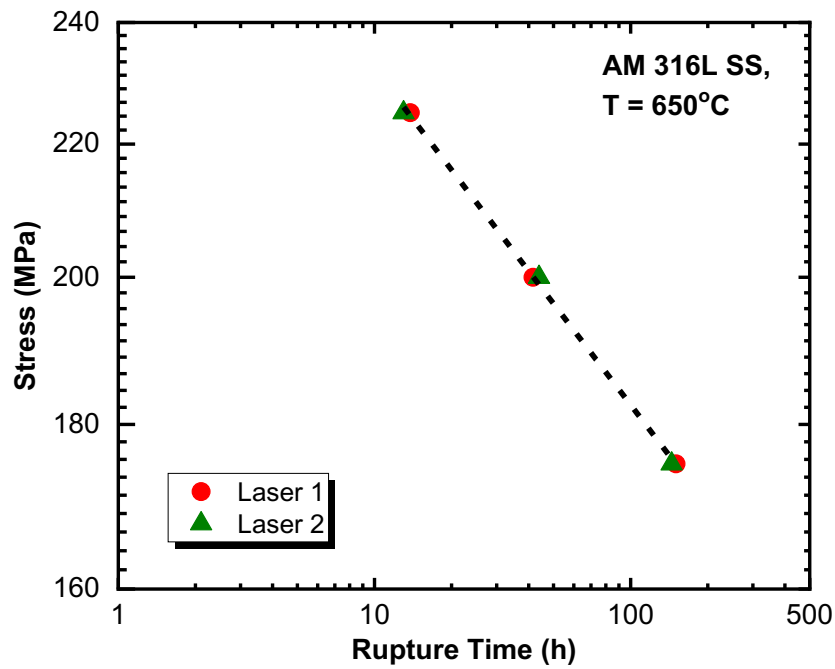


Figure 31. Stress-rupture time plot for AM 316L (Build 20190308) tested at 650°C.



Figure 32. Photographs of the AM 316L (Build 20190308) creep-ruptured specimens.

Table 8. Creep test data of AM 316L (Build 20190308).

Sample ID	AM condition	Stress (MPa)	Temp (°C)	Rupture time (h)	Min. creep rate (1/s)	Creep rupture strain (%)	R.A. (%)
L101	Laser 1	225	650	13.8	$1.22 \times 10^{-6}$	46.9	45.1
L102	Laser 1	200	650	41.6	$2.59 \times 10^{-7}$	40.7	43.0
L103	Laser 1	175	650	150.3	$6.41 \times 10^{-8}$	45.8	44.2
L201	Laser 2	225	650	13.0	$1.39 \times 10^{-6}$	47.5	46.0
L202	Laser 2	200	650	43.9	$2.53 \times 10^{-7}$	53.5	46.9
L203	Laser 2	175	650	144.5	$6.61 \times 10^{-8}$	43.2	44.2

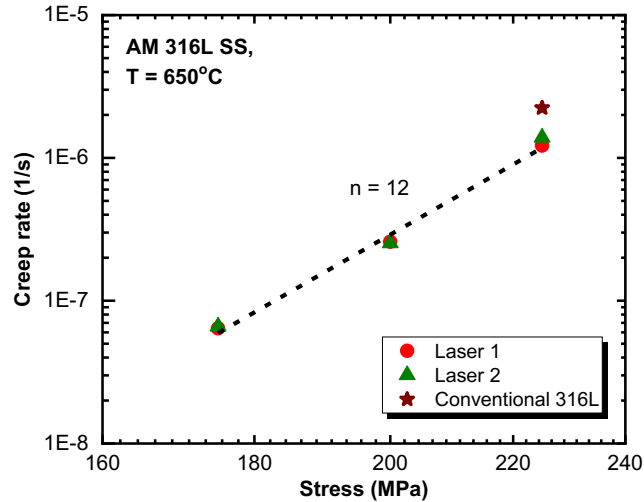


Figure 33. The minimum creep rate vs. applied stress for AM 316L (Build 20190308) tested at 650°C.

Figure 34 compares the creep curves of AM 316L (Build 20190308) in the as-printed condition with the conventional 316L tested at 650°C, 225 MPa. AM316L SS shows shorter rupture times than conventional 316L SS. In contrast to AM316L, which exhibited accelerated creep, conventional 316L had distinct primary, steady-state, and tertiary creep. The steady-state creep rate of conventional 316L is higher than the minimum creep rate of AM316L, as shown in the figure.

A broken half of the creep-ruptured specimen was sectioned along the specimen gauge. It was ground, polished, and etched for examinations by optical microscopy. Figure 35 shows the optical micrographs, taken near the fracture region in the longitudinal direction, of creep-ruptured specimens for AM 316L and conventional 316L, respectively, after the creep tests at 650°C, 225 MPa. Significant wedge-type cracking at grain boundary triple points was observed in conventional 316L. While grain boundary cracking was also evident in AM 316L, that specimen showed a higher density of cracks with small sizes, likely due to the smaller and often elongated or bent grains in AM 316L relative to large grains in annealed conventional 316L. The as-received AM 316L needs to be examined to separate creep voids and porosity formed during printing.

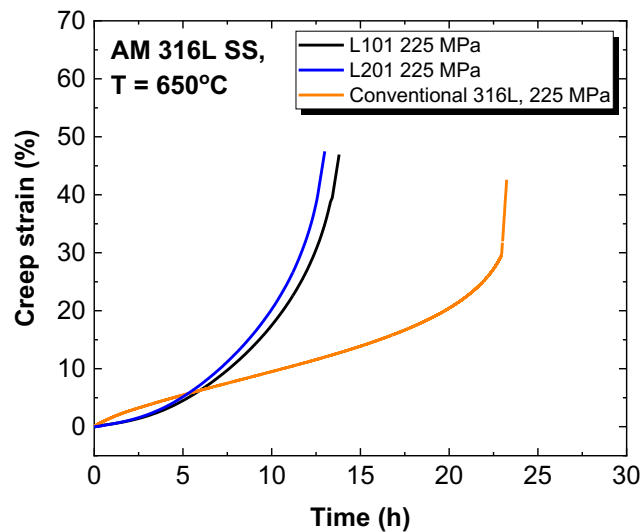
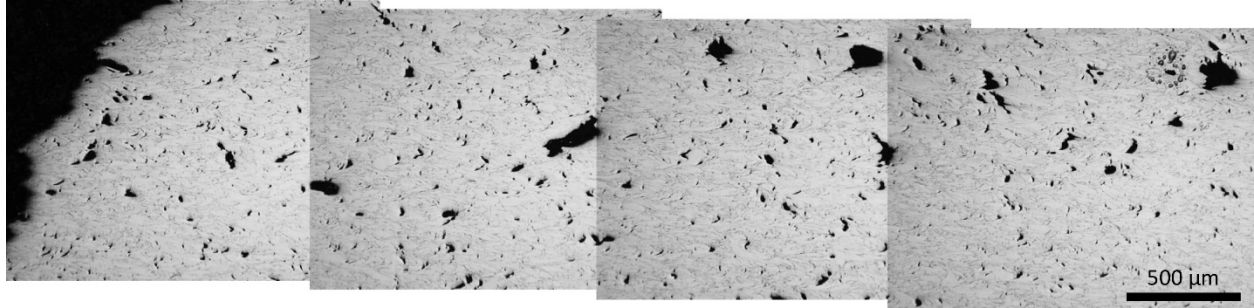
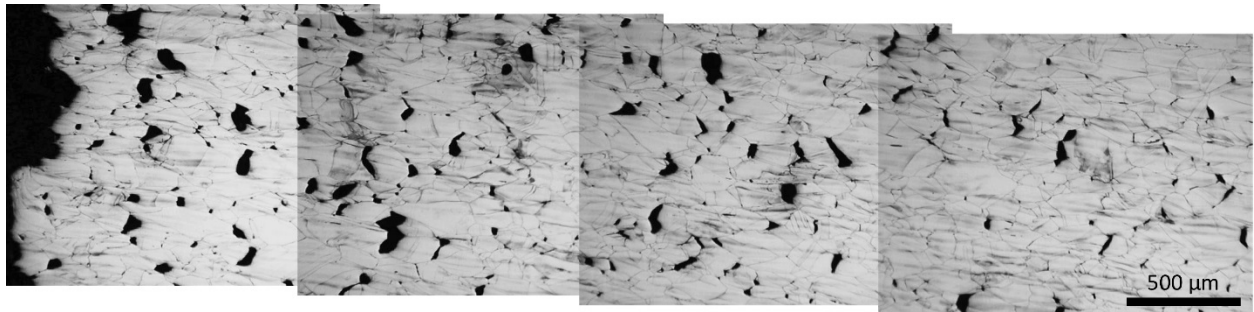


Figure 34. Creep curves of AM 316L (Build 20190308) and conventional 316L tested at 650°C, 225 MPa.



**AM 316L SS (650°C, 225 MPa)**



**Conventional 316L SS (650°C, 225 MPa)**

**Figure 35. Optical micrographs near the fracture region of the creep-tested specimens in the longitudinal direction AM 316L (top) and conventional 316L (bottom) stainless steels creep tested at 650°C, 225 MPa.**

### **3.5.9 Fatigue**

The fatigue properties of ORNL-derived 316L have not been studied to date.

### **3.5.10 Fretting and wear**

The fretting and wear properties of ORNL-derived 316L have not been studied to date.

## 4. SiC PRODUCED USING BINDERJET PRINTING AND CVI

### 4.1 GENERAL MATERIAL PROPERTIES AND MICROSTRUCTURE

The microstructure of the binderjet-printed and chemical vapor–infiltrated SiC is shown in Figure 36, which shows the 3D printed SiC powder embedded in a continuous matrix of CVI SiC with some porosity. The CVI process densifies the part until all the pores are closed. As expected, the final density with remaining close porosity reaches 90–92% of theoretical density of SiC ( $3.2 \text{ g/cm}^3$ ). The density for the various specimens was measured using the Archimedes method.

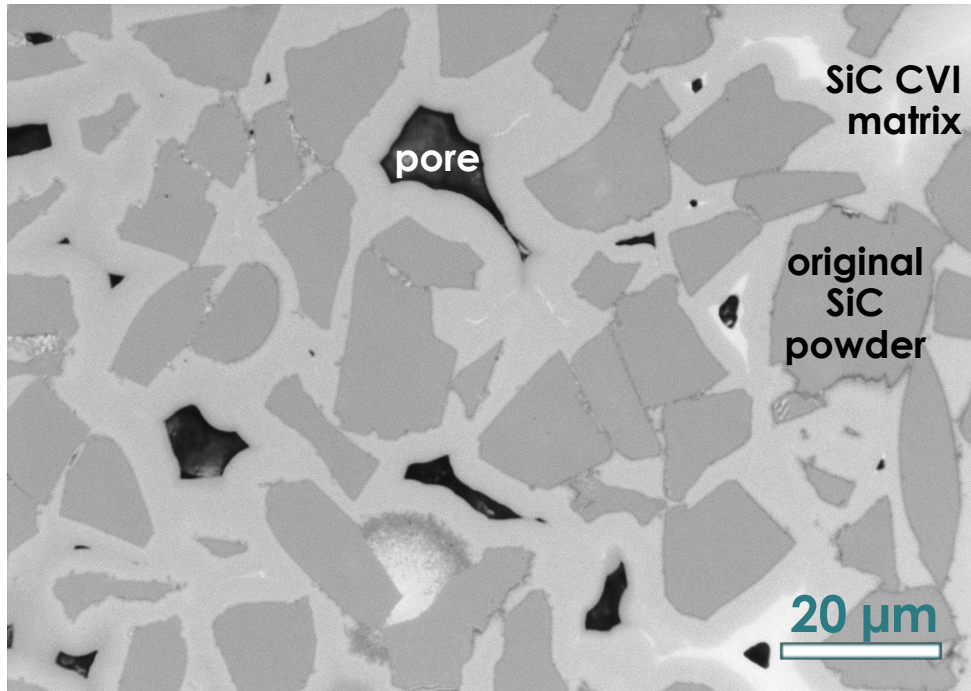


Figure 36. Optical micrograph of the cross section of binderjet printed and chemical vapor–infiltrated SiC.

### 4.2 THERMAL PROPERTIES

The thermal diffusivity of the 3D printed SiC was measured using the laser flash methodology. The 3D printed disks of 12.5 mm diameter and 1.9 mm thick were examined using a Netzsch LFA 467 Hyper Flash instrument per ASTM E1461 (Figure 37). Thermal conductivity, which was calculated using the measured diffusivity and density and heat capacity for pure SiC [9] is shown in Figure 38.

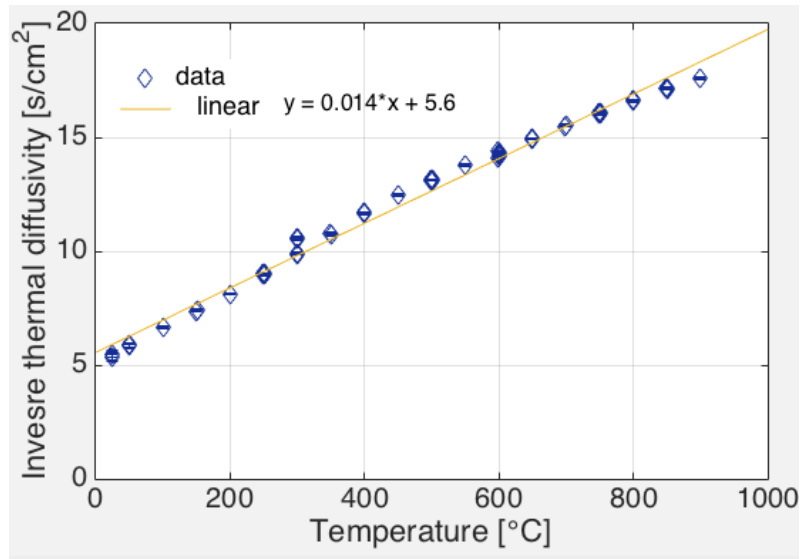


Figure 37. Inverse thermal diffusivity measured on 3D printed SiC.

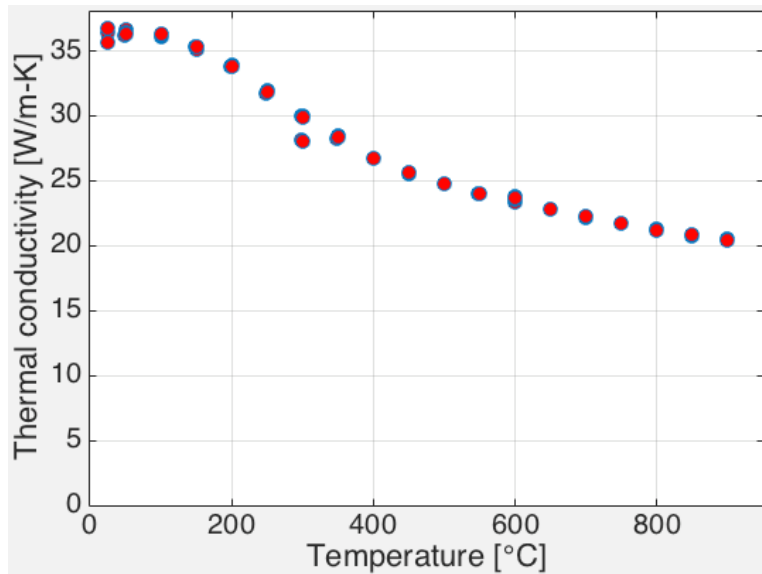


Figure 38. Calculated thermal conductivity of 3D printed SiC.

### 4.3 MECHANICAL PROPERTIES

The strength of 3D printed SiC for the fuel matrix or as TCR core structural component is of high importance. These components will be exposed to a temperature gradient that in turns results in a swelling and stress gradient, as described in detail in Ben-Belgacem et al. [10]. Since monolithic SiC is inherently brittle, a statistical approach to failure is necessary. To inform this approach, monotonic equi-biaxial flexure testing was conducted on 3D printed SiC specimens in conformance with ASTM C1499-05. The disks were 6 mm in diameter and 0.48 mm thick. The surfaces of the disks were smooth because they were ground using a diamond abrasive wheel after the CVI densification step. Figure 39 shows the results of these tests alongside data from a reference material, i.e., high-density bulk chemical vapor-deposited SiC taken from Kondo et al. [11]. The failure probability based on the fit of the data in Figure 39 is plotted in Figure 40.

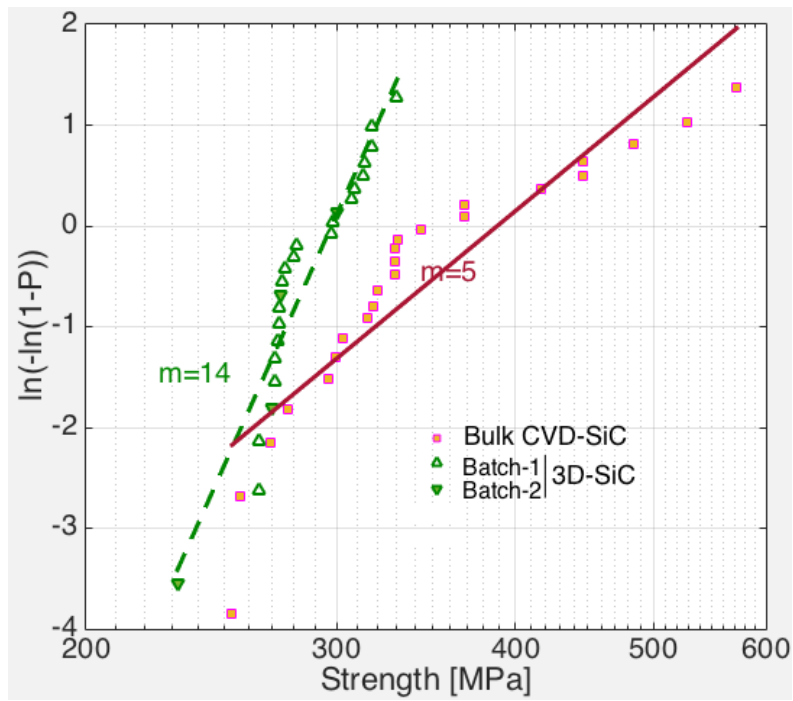


Figure 39. Weibull plot of SiC fracture strength from monotonic equi-biaxial flexure testing. Results from bulk CVD-SiC are from Kondo et al. [11]. “P” is failure probability.

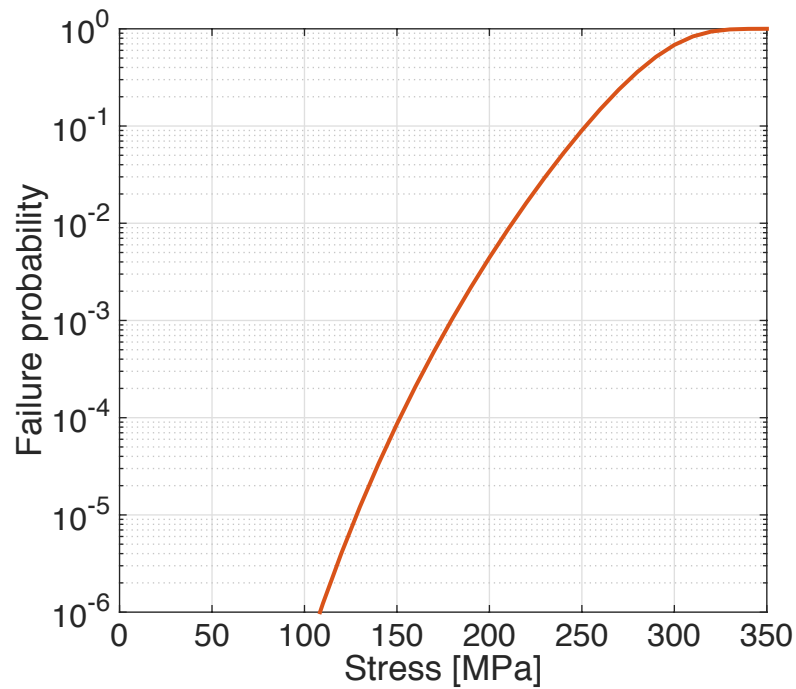


Figure 40. Failure probability for 3D printed SiC based on equi-biaxial flexure strength data. The data should be normalized for an effective test volume of 1.57 mm<sup>3</sup>.

## 5. CONCLUSIONS

The transformational challenge reactor (TCR) program is employing additive manufacturing technologies to produce a small nuclear core with structural materials including SiC and Grade 316L austenitic stainless steel. A database of the properties of these AM materials, including their thermophysical and mechanical properties, is required to inform the design and safety analysis of the TCR core and reactor system. This report provides a compilation of material properties data derived from additively manufactured 316L and SiC builds at ORNL within FY 2019. This data handbook is being and will be used for design refinement and safety analysis work in the coming years and will be updated on an annual basis.

## 6. REFERENCES

- [1] K. Terrani, B. Jolly, M. Trammell, 3D printing of high-purity silicon carbide, *J. Am. Ceram. Soc.* submitted (2019).
- [2] T. DebRoy, H.L. Wei, J.S. Zuback, T. Mukherjee, J.W. Elmer, J.O. Milewski, A.M. Beese, A. Wilson-Heid, A. De, W. Zhang, Additive manufacturing of metallic components—process, structure and properties, *Prog. Mater. Sci.* 92 (2018) 112–224.
- [3] C.S. Kim, Thermophysical properties of stainless steels, ANL-75-55. (1975).
- [4] M.N. Gussev, J.T. Busby, K.G. Field, M.A. Sokolov, S.E. Gray, Role of scale factor during tensile testing of small specimens, in: *ASTM Spec. Tech. Publ.*, 2015. doi:10.1520/STP157620140013.
- [5] J.W. Davis, *ITER Materials Properties Handbook*, ITER Doc. No. S74 MA 2 97-12-12 R 0.2. (1997).
- [6] B.A. Pint, K.A. Terrani, Severe Accident Test Station Activity Report, Oak Ridge, TN (United States), 2015. doi:10.2172/1186001.
- [7] H. Yamada, Failure of type 316 stainless steel cladding during thermal transients, *J. Nucl. Mater.* 78 (1978) 24–32.
- [8] C.P. Massey, K.A. Terrani, S.N. Dryepndt, B.A. Pint, Cladding burst behavior of Fe-based alloys under LOCA, *J. Nucl. Mater.* 470 (2016) 128–138.
- [9] L.L. Snead, T. Nozawa, Y. Katoh, T.S. Byun, S. Kondo, D.A. Petti, Handbook of SiC properties for fuel performance modeling, *J. Nucl. Mater.* 371 (2007) 329–377.
- [10] M. Ben-Belgacem, V. Richet, K.A. Terrani, Y. Katoh, L.L. Snead, Thermo-mechanical analysis of LWR SiC/SiC composite cladding, *J. Nucl. Mater.* 447 (2014). doi:10.1016/j.jnucmat.2014.01.006.
- [11] S. Kondo, Y. Katoh, L.L. Snead, Concentric ring on ring test for unirradiated and irradiated miniature SiC specimens, *J. Nucl. Mater.* 417 (2011) 406–410.

